Transport Properties of the LaInO$_3$/BaSnO$_3$ Interface Analyzed by Poisson-Schrödinger Equation

Youjung Kim[,1] Seonghyeon Kim[,1] Hyeongmin Cho[,1] Young Mo Kim,[1,†] Hiromichi Ohta[,2] and
Kookrin Char[1,*]

[1]*Department of Physics and Astronomy, Institute of Applied Physics, Seoul National University, Seoul 08826,
Korea*
[2]*Research Institute for Electronic Science, Hokkaido University, N20W10, Kita, Sapporo 001-0020, Japan*

2DEG systems formed in quantum wells of semiconductor heterostructures have been instrumental in advancing science and technology for many decades. Here, we report two unique transport properties of 2DEG formed at the interface of two perovskite oxides LaInO$_3$ (LIO) and BaSnO$_3$ (BSO): the peculiar LIO thickness dependence of the high two-dimensional (2D) carrier density (n_{2D}) and the very narrow width of the quantum well. We analyze, via Poisson-Schrödinger simulation, how the various materials parameters affect the 2D carrier density and its profile when using the "interface-polarization" model in which the polarization exists only near the interface. Our simulations show that the known material parameters of LIO and BSO are capable of generating a deep and narrow quantum well as suggested by the experimental transport properties and reveal some distinct features of the LIO/BSO interface from the conventional 2DEGs. Furthermore, they predict how the LIO/BSO 2DEG will evolve as the defect density decreases.

I. INTRODUCTION

2DEG systems have been studied in several material systems because of their applicability to devices such as HEMT [1] and interesting physical properties such as quantum phenomena [2]. There are well-known 2DEG heterostructures such as (AlGa)As/GaAs, (AlGa)N/GaN, and (MgZn)O/ZnO with high two-dimensional carrier density (n_{2D}) and high mobility, which form triangular quantum wells near the interface [3–5]. In recent years, perovskite oxide interfaces have been found to exhibit even higher n_{2D} while the conventional 2DEGs have less than 1×10^{13} cm^{-2} at the (AlGa)N/GaN [3,6] and (MgZn)O/ZnO [4,7] interfaces and 1×10^{11} cm^{-2} at the (AlGa)As/GaAs interface [5,8]. For example, the LaAlO$_3$(LAO)/SrTiO$_3$(STO) oxide interface in a perovskite structure showed n_{2D} of 1×10^{13}–3×10^{14} cm^{-2} [9,10]. The n_{2D} of LaInO$_3$(LIO)/BaSnO$_3$(BSO) 2DEG have been reported to be about 1×10^{13}–3×10^{13} cm^{-2} [11,12] in spite of a large dislocation density in the BSO channel acting as deep acceptors. High n_{2D} is a factor in creating high drain current and transconductance in HEMT and such a high density of carriers at the perovskite oxide interfaces can be completely modulated when combined with the high dielectric material of the same perovskite structure [13].

The formation of 2DEGs is generally understood in terms of band bending created by the conduction-band offset at (AlGa)As/GaAs ("modulation doping") [14] and the discontinuity of spontaneous and/or piezoelectric polarization at (AlGa)N/GaN and (MgZn)O/ZnO ("polarization doping") [3,4], which can explain the dependence of the electrical properties on the thickness of the wider band-gap semiconductor [15–19]. On the other hand, a "polar catastrophe" model with a "charge-transfer" process through a specific termination layer has been proposed as a primary mechanism for the LAO/STO interface [20], although there are many inconsistent reports on its mechanism, for example, cation diffusion and oxygen-vacancy formation [21]. In the LIO/(Ba, La)SnO$_3$ (BLSO) interface, such possibilities as cation diffusion and oxygen vacancies were ruled out by a series of experiments [11] with the help of its high oxygen stability [22]. For the LIO/BSO interface an "interface-polarization" model that the polarization exists only near the interface, rapidly decreasing beyond 2 unit cells of LIO from the interface, was proposed to describe the formation of a quantum well and the peculiar LIO thickness-dependent n_{2D}, which shows totally different characteristics from the conventional 2DEGs [23]. The polarization exists only near the interface since the bulk cubic and orthorhombic perovskite oxides cannot possess polarization due to their inversion

―――――
*kchar@snu.ac.kr
†Present address: SK Hynix Research, Icheon-si, Gyongki-do, Korea.

symmetry. This is in contrast to the conventional 2DEGs where the absence of inversion symmetry can create spontaneous and piezoelectric polarizations over a long length scale aided by the lattice strain [24]. The inversion symmetry breaking at the interface of orthorhombic LIO and the cubic BSO perovskite oxide is believed to be capable of "interface polarization" [25].

Theoretically, 2DEG systems have been analyzed through calculations using the one-dimensional (1D) Poisson-Schrödinger (PS) equation to investigate how the semiconducting material parameters affect formation of the quantum well and its n_{2D}. The PS equation is a widely used tool to predict the band bending of systems such as nanowires, diodes, transistors, and 2DEGs [26–29] by calculating the modified potential energy from the changes in charge distribution. The calculation results for the three conventional 2DEGs, shown in our Appendix, considering the conduction-band offset and the polarization discontinuity as the origin of 2DEG at the interface, agree well with the experimental results showing the quantum well with n_{2D} of 1×10^{11} cm^{-2} in the GaAs interface [30] and about 1×10^{13} cm^{-2} n_{2D} in the GaN [31] and ZnO [32] interface. It also provides insight into how the changing material parameters affect the 2DEG properties. In a modulation-doped (AlGa)As/GaAs 2DEG system, the effects of boundary conditions and the deep donors on the quantum well were investigated [33,34]. The properties of the polarization-doped (AlGa)N/GaN 2DEG were correlated with the background donor concentration and surface boundary conditions, and we found the surface boundary conditions to be the most crucial parameter [31]. The n_{2D} of (MgZn)O/ZnO 2DEG was found to be dependent on the Mg composition, the (MgZn)O layer thickness, and the surface state density [32,35,36].

There have been attempts to simulate the LAO/STO interface using PS formalism by directly placing a large density of donors right at the interface to mimic the "charge transfer" or the La-diffusion mechanism [37,38]. By using the same method, 2DEG possibility was suggested for the LIO/BSO interface [39]. However, as more experimental data become available, in particular, the LIO thickness-dependent n_{2D}, it has become clear that such an approach of directly placing a large donor density is inadequate to explain the experimental LIO thickness-dependent n_{2D} data. In this paper, we first report on two experimental data sets: the LIO thickness-dependent n_{2D} on MgO substrates and its thermopower measurement. Subsequently, we report on the PS simulation of the interface, focusing on the LIO thickness-dependent n_{2D} and its profile. In our simulation we investigate how the behavior of n_{2D} changes quantitatively depending on the material parameters using the "interface-polarization" model, since it is the only model available that can explain the LIO thickness-dependent n_{2D}. The main goal of the paper is to understand how the varying material parameters affect the 2DEG and show what the most useful material parameters are for 2DEG formation at oxide interfaces. The material parameters of interest are polarization, concentration, and activation energy of shallow and deep carriers, effective mass, dielectric constants, and conduction-band offset between LIO and BSO. Finally, we show that the narrow width of the quantum well indicated by the thermopower measurement is consistent with our PS simulation results.

II. EXPERIMENTAL TRANSPORT PROPERTIES

The two unique transport properties of the LIO/BLSO interface are experimentally obtained. First, from the structure of Fig. 1(a), as we change the LIO thickness, high n_{2D} of the interface with peculiar trend in its LIO thickness dependence is measured. All layers of the sample are deposited by the pulsed-laser deposition technique. Targets are ablated for deposition with an energy fluence of approximately 1.5 J/cm^2 using a 248-nm wavelength KrF excimer laser at 750 °C in 0.1 Torr oxygen pressure. All targets are manufactured by Toshima Manufacturing Co. in Japan. A Keithely 4200SCS parameter analyzer is used to record the electrical properties. MgO is chosen as the substrate for the better property of the BLSO channel layer, which have lower density of deep acceptors that trap electrons [40] as well as for the excellent insulating property of the substrate itself, rendered by its larger band gap [12] and much less propensity to form oxygen vacancies, than STO substrates. The LIO/BLSO interface on the MgO substrate is deposited with the BaHfO$_3$ (BHO) and BSO buffer layers to reduce the dislocation density by alleviating the lattice mismatch problem with the substrate [12]. For the channel layer, a 0.2% La-doped BSO layer with insulating property is used. While changing the thickness of the LIO layer on the 0.2% La-doped BSO channel layer, the Hall measurement of the interface is performed in Van der Pauw geometry through a contact layer of metallic 4% La-doped BSO in the four corners of the samples.

The conductance of the interface rapidly increases as soon as the first unit cell of LIO is deposited [11,12]. After increasing by several orders of magnitude, the interface conductance reaches the maximum conductance of about 1×10^{-4} Ω^{-1} at the 4 unit-cell thickness of LIO. Beyond 4 unit-cell thickness of LIO, the interface conductance decreases and starts to saturate around 5 nm thickness. This trend is very robust and consistent, independent of the substrate type (STO or MgO). Recently, even the Ga-alloyed LIO/BLSO interfaces were reported to show the same trend (increasing, decreasing, and saturating), although the magnitudes became smaller as the Ga alloying ratio increased [25].

Since it is n_{2D} that can be calculated by a model, in this paper we focus on the magnitude of n_{2D} and its profile. The n_{2D} of the interface at each LIO thickness are indicated by red points in Fig. 1(b). The n_{2D} increases
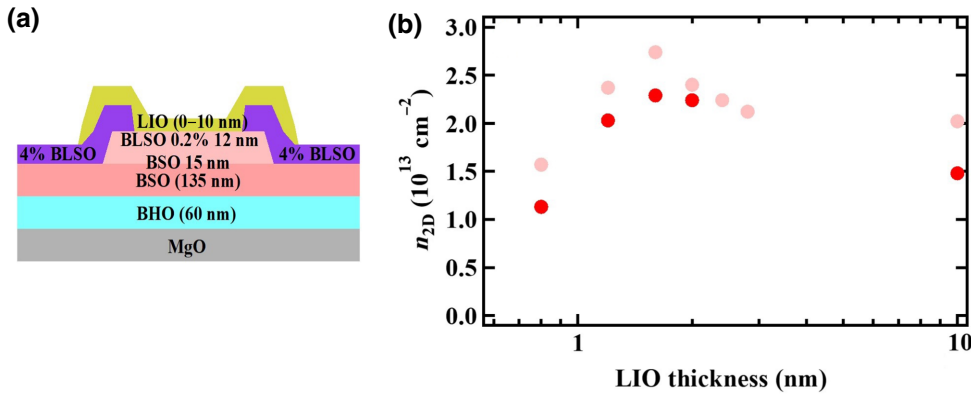
FIG. 1. Experiments to measure the 2D carrier density (n_{2D}) of the LIO/BLSO interface (a) LIO/BLSO schematic structure with buffer and contact layers. (b) n_{2D} of the interface at each LIO thickness in red dots, with the 0.2% doped channel on MgO substrates. The pink dots are for comparison with data of the 0.3% doped channels on STO substrates from Ref. [23].

as the LIO thickness increases from 1 unit cell to 4 unit cells, and after the peak value at 4 unit-cell thickness, it decreases and saturates, following the behavior of the interface conductance. This LIO thickness dependence is the most peculiar properties of the LIO/BLSO interface, uniquely different from those of other conventional 2DEGs. The exact same trend in its LIO thickness dependence is seen in our previous reports of the LIO/BLSO interface on STO substrates, which are represented in pink dots. In order to explain this unique property, we devise the "interface-polarization" model [23]. The highest n_{2D}, 2–3×10^{13} cm^{-2}, is larger than those of conventional 2DEGs, although the LIO/BLSO interface is grown heteroepitaxially on MgO substrates with a large lattice mismatch, which generates large density threading dislocations that act as deep acceptors, lower the electron density, and reduce the mobility.

For the second transport property, the thermopower is measured using a sample made with the same process and structure as the sample in Fig. 1, except the use of the undoped channel layer. Unlike electrical conductance measurement, thermopower is sensitive only to its carrier density, three-dimensional (3D) or two-dimensional (2D), independent of its mobility. At room temperature, the thermopower S is measured with a maximum temperature difference of 3 K across the film, generated by two Peltier devices, as shown in Fig. 2(a). Two thermocouples monitored the actual temperatures, measuring thermoelectromotive forces simultaneously. More details of the measurement are provided in Ref. [41]. The thermopower is obtained from the variation of the thermoelectromotive force as a function of the temperature difference, as described in Fig. 2(b). It displays the thermopower value of -73 μV K^{-1}. The relation between thermopower and the carrier density in BLSO film has been studied in detail previously both in 3D and 2D cases [41]. The 2D cases were measured by using a field effect through a gate oxide layer. Since the conducting layer in the LIO/BSO interface is the BSO layer [23], the measured property of thermopower of the LIO/BSO interface should be consistent with that of BLSO film. The measured thermopower of

-73 μV K^{-1} corresponds to 1.8×10^{20} cm^{-3} in 3D and 1.2×10^{13} cm^{-2} in 2D. From this, we can estimate another parameter of the LIO/BSO interface, namely the width (or the thickness) of the channel layer at the LIO/BSO 2DEG, which is 1.2×10^{13} cm^{-2} divided by 1.8×10^{20} cm^{-3}, to be about 1 nm. This very narrow width of quantum well is another unique property in comparison to the conventional 2DEGs. Although we have not yet seen a 2D quantum phenomenon directly due to the dislocation-limited mobility at low temperatures, it indirectly shows that a very narrow 2D quantum well forms. We now try to explain these two unique transport properties by simulating the interface in PS formalism by using semiconductor physics plus "interface polarization."

III. PS SIMULATIONS AND ANALYSIS

For our simulations by PS formalism, we employ the PS band calculator designed by Snider [29] (freely available at http://www3.nd.edu/ gsnider/). In order to validate our method for simulations, we first calculate, in the Appendix, the n_{2D} of conventional 2DEGs, namely (AlGa)As/GaAs, (AlGa)N/GaN, and (MgZn)O/ZnO. The n_{2D} values we obtain are found to be consistent with the experimental values available.

For our perovskite oxide LIO/BLSO interface, we use the same PS simulations with one key difference from the conventional 2DEGs. Instead of spontaneous and piezoelectric polarizations in the cases for (AlGa)N/GaN, and (MgZn)O/ZnO systems, we use "interface polarization," which exists only near the interface. Previously, we showed that only by introducing the "interface polarization" could we explain the characteristics of LIO thickness-dependent n_{2D} that has a peak value at a 4 unit-cell thickness of LIO [23]. This characteristic cannot be explained using "constant polarization" typically used for conventional 2DEGs (GaN and ZnO systems) that shows monotonic increase of n_{2D} with a much larger thickness scale (tens of nm) when the thickness of the wider band-gap materials, (AlGa)N and (MgZn)O, increases [17–19].
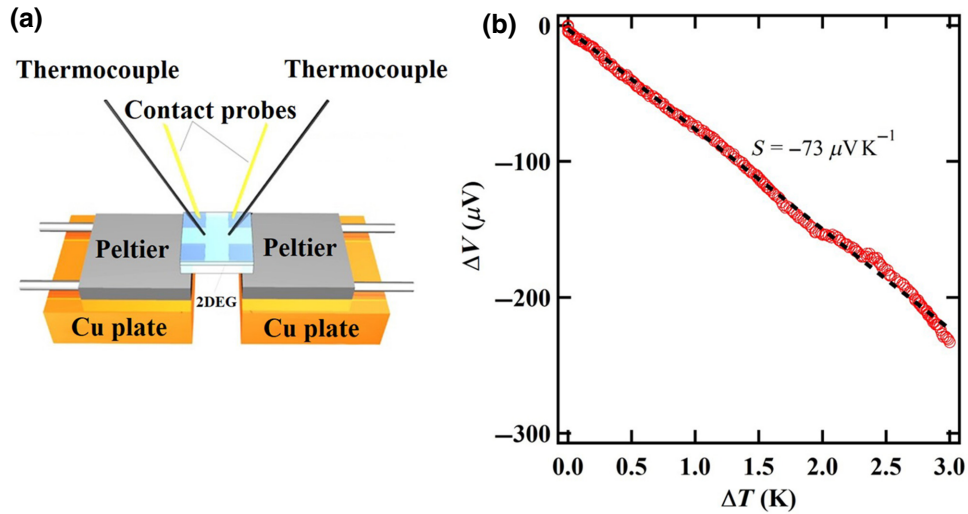
FIG. 2. Thermopower measurement. (a) Experimental setup. The 2DEG sample is placed between the gap of two Peltier devices (one is cooler, the other one is hotter), which is used to generate a temperature difference (ΔT). The ΔT is measured using two tiny K-type thermocouples placed at the edge of the electrodes. The thermoelectromotive force (ΔV) is measured using a digital multimeter. (b) Thermoelectromotive force as a function of temperature difference at the LIO/BSO (undoped) interface that shows thermopower of $-73\ \mu\mathrm{V\,K^{-1}}$.

To date, direct evidences for such "interface polarization" are the highly strained interface structure between the cubic BSO and orthorhombic LIO, observed by TEM [23] and by synchrotron x-ray diffraction [42], showing modification in octahedral tilting over a range of a few unit cells of LIO near the interface. Very recently, it has been reported that the orthorhombic-cubic strain at the Ga-alloyed LIO/BSO interface via coherent epitaxy is closely related to the interface polarization [25]. In a similar interface of the orthorhombic and cubic structure of SrRuO$_3$/STO, symmetry breaking near the interface was also measured, which was found to enable polarization [43].

Based on these grounds, using the "interface-polarization" model, we perform simulations at a temperature of 300 K. Several material parameters and boundary conditions are key factors in calculation using the PS equation. All the material parameters used in the calculation are listed in Table I. They are the effective mass (m_e^*/m_0), the dielectric constant (κ), the band gap (E_g), the conduction-band offset (ΔE_C), the polarization (P), the donor density and its activation energy (N_D, E_D), the acceptor density and its activation energy (N_A, E_A), the deep-donor density and its activation energy (N_{DD}, E_{DD}), and the deep acceptor and its activation energy (N_{DA}, E_{DA}), some of which are obtained from experiments [23,44–49]. Our goal here is to see how robust the two unique transport properties are when the material parameters mentioned above change in our PS simulation.

Among them, the polarization near the interface and the deep-donor density of LIO are two unknown parameters that we deduce from the experimental results.

Without any knowledge on the activation energies of the LIO deep donors and the BSO deep acceptors, as a starting point, we place them at the center of the band gap for simplicity. Simultaneously, the deep acceptors in LIO and the deep donors of BSO are not considered as they are never activated because the Fermi level is lower than the deep acceptor level in LIO and higher than the deep-donor level in BSO when band bending is induced by the conduction-band offset and polarization at the interface. In most of cases, the "Ohmic" boundary conditions are used at the LIO surface and the BSO bottom surface. The "Ohmic" boundary condition sets the charge neutrality condition that the Fermi level locates in the middle of the band gap, which is exactly the level of the deep carriers of LIO and BSO. Many of the calculations are done with

TABLE I.   Material parameters used for BSO and LIO.

	BSO	LIO
m_e^*/m_0	0.42	0.46
κ	20	38
E_g (eV)	3.1	5.0
ΔE_C (eV)	–	1.6
P (μC cm^{-2})	0	$P_{\mathrm{int}} = 60/60/25/10$
N_D (cm^{-3}), E_D (eV)	1.43×10^{19} (for 0.1% La doping), -0.63	–
N_A (cm^{-3}), E_A (eV)	–	–
N_{DD} (cm^{-3}), E_{DD} (eV)	–	1.3×10^{20}, 2.5
N_{DA} (cm^{-3}), E_{DA} (eV)	4×10^{19}, 1.55	–
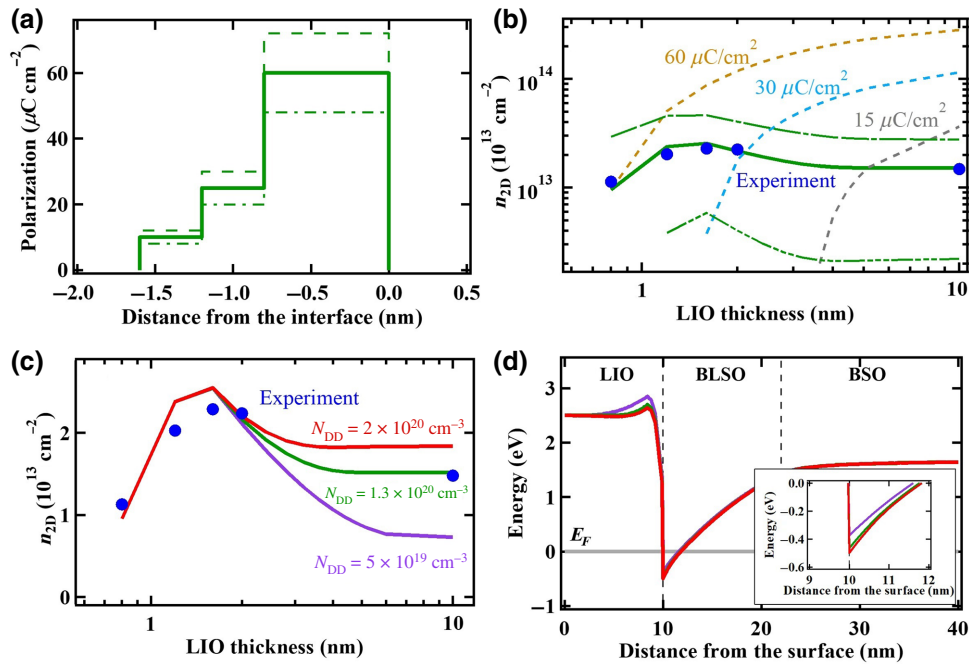
FIG. 3.   Results of PS calculations to define the unknown polarization value and deep-donor density in LIO at the LIO/BLSO interface. (a) Interface-polarization values on the LIO side that fits the experimental results. (b) Carrier densities of the quantum well calculated using the interface polarization in (a) are drawn by the green solid lines that explains the experimental result of the blue dots. Increased and decreased carrier densities of thin green lines from the green solid line are calculated using the polarization values that are increased and decreased 20% from the thick solid green line of (a). Carrier densities using constant polarizations in the entire LIO film are shown as dashed lines, which cannot explain the experimental data. (c) Carrier densities of the quantum well in the cases of LIO deep-donor densities of 5×10^{19} cm^{-3}, 1.3×10^{20} cm^{-3}, and 2×10^{20} cm^{-3} using the interface polarization of the solid green line in (a). The blue dots are experimental results. (d) Changes in minimum conduction-band bending at each deep-donor density of LIO at LIO 10 nm. The quantum well is enlarged in the inset.

0.2% La-doped BLSO in line with the experiment. Since the density of the deep acceptors in BSO is higher than the La-doping rate, 0.2% La-doped BLSO itself is insulating. However, some calculations used the undoped BSO channel due to the difficulty of calculating very large carrier density especially when BSO is set to have a small density of deep acceptors or the activation energy of the deep donors in LIO is set to be small in Figs. 3–5.

A. Polarization and deep-donor density in LIO

First, we set the two completely unknown parameters: the magnitude of the interface polarization and the deep-donor density in LIO to fit the experimentally obtained n_{2D} at the interface. For a rough guess on polarization and deep-donor density, we first try the similar values adopted for the LIO/BLSO interface grown on STO substrates [23] and find the interface-polarization values that can fit the experimental data on MgO substrates in Fig. 1 by slightly adjusting the values. The interface polarization is described by a thick solid line in Fig. 3(a): 60 μC cm^{-2} in the first two unit cells, 25 μC cm^{-2} in the third unit cell, 10 μC cm^{-2} in the fourth unit cell, and 0 μC cm^{-2}

thereafter from the interface (60/60/25/10 μC cm^{-2}). The calculation values of n_{2D} with these polarization values are indicated by the solid green line in Fig. 3(b) and they fit well with the experimental results. The use of a different type of substrate and slightly different deposition conditions seem to produce slightly different polarization values from our previous report [23]. The deep-donor density used for LIO is 1.3×10^{20} cm^{-3} here. Such interface polarization is consistent with the unique thickness-dependent n_{2D} in LIO/BLSO, which has a maximum value at 4 unit cells of LIO. The inversion symmetry in orthorhombic LIO precludes the bulk polarization in LIO. However, it is possible that the inversion symmetry is broken at the interface with the aid of strain and octahedral tilting.

We try to see how much a 20% change in the polarization values will change the n_{2D}. The two kinds of dashed (long dashed and dot dashed) green lines in Fig. 3(b) represent the change in n_{2D}. From the n_{2D} results at each polarization, it is easy to understand that higher polarization makes higher electric field, deeper quantum well, and higher n_{2D}, which is the first transport property of the LIO/BSO interface while conventional 2DEGs have low polarization values. The polarization value calculated
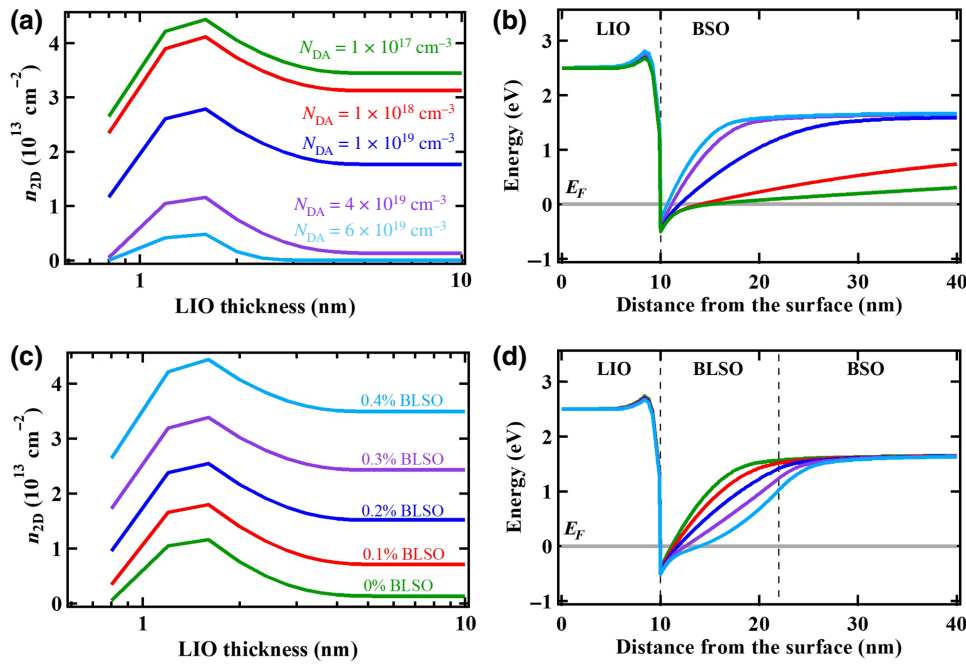
FIG. 4. Influence of the deep-acceptor density and La-dopant density of BSO on the LIO/undoped BSO and the LIO/BLSO interface calculated with the PS equation. (a) n_{2D} of the quantum well with a deep-acceptor density of 1×10^{17} cm^{-3}, 1×10^{18} cm^{-3}, 1×10^{19} cm^{-3}, 4×10^{19} cm^{-3}, and 6×10^{19} cm^{-3} as a function of the LIO thickness. (b) Changes in conduction-band bending at each deep-acceptor density in BSO with LIO 10 nm. (c) n_{2D} of the quantum well with La-donor density from 0 to 5.72×10^{19} cm^{-3} (0.4% BSLO) as a function of the LIO thickness. (d) Changes in conduction-band bending at each La-donor density in BSO at LIO 10 nm.

from the alternating layers of $(LaO)^+$ and $(InO_2)^-$ is about 55 μC cm^{-2}. The dashed lines in different colors are the results of assuming a constant polarization throughout the LIO with three different polarization values: 60, 30, and 15 μC cm^{-2}. They show a monotonic increase of n_{2D}, the same trend as in GaN and ZnO-based 2DEG [17–19].

Using the interface-polarization values of 60/60/25/10 μC cm^{-2} that fit with the experimental results, we are now ready to see the effect of the deep-donor density in LIO. Figure 3(c) presents the n_{2D} of the interface as a function of the LIO thickness in the cases of three deep-donor densities in LIO: 5×10^{19}, 1.3×10^{20}, and 2×10^{20} cm^{-3} represented by purple, green, and red lines, respectively. The green line in Fig. 3(c) is the same as the solid green in Fig. 3(b). The experimental results of n_{2D} at 10 nm LIO thickness fit well with the calculation result with 1.3×10^{20} cm^{-3} of LIO deep-donor density while the experiments on STO substrates agreed with 2×10^{20} cm^{-3} deep-donor density in LIO [23]. The difference in LIO deep-donor density affects only the n_{2D} for the LIO thickness beyond 4 unit cells, after the interface polarization ends at the LIO. This is because the deep donors near the interface are not ionized due to insufficient band bending [23]. This can be explained better using Fig. 3(d).

The conduction-band minimums are presented in Fig. 3(d) in the case of each LIO deep-donor concentration with 10 nm LIO thickness. The potential of the interface polarization in LIO renders the energy of the LIO side (8.4 nm of x axis) higher and the BSO side (10 nm of x axis) lower. Since the deep donors become activated only when the deep-donor level is higher than the Fermi level, the deep-donor states near the interface remain

unactivated. After sufficient band bending by the interface polarization, the deep donors will become activated and the remaining positive ions will start screening the ending polarization. As shown in Fig. 3(d) and its inset, smaller deep-donor density in LIO provides less screening, resulting in higher conduction-band energy, shallower quantum well, and smaller n_{2D} in the thick LIO limit. In contrast, a larger deep-donor density provides more screening, resulting in lower conduction band, deeper quantum well, and higher n_{2D}, as previously described in Ref. [23]. If such deep donors are due to the most likely oxygen vacancies in LIO, 1.3×10^{20} cm^{-3} density corresponds to LaInO$_{2.996}$ instead of stoichiometric LaInO$_3$.

B. Deep acceptor and La-donor densities in BSO

Since we pick two unknown parameters in LIO (the polarization and the deep-donor density) and show that an "interface-polarization" model is consistent with the thickness-dependent n_{2D} described in Fig. 1, for the remaining part of the paper we are going to fix the polarization value to be 60/60/25/10 μC cm^{-2} in each unit cell of the four unit cells of LIO at the interface and the deep-donor density in LIO to be 1.3×10^{20} cm^{-3}. We investigate how other material parameters will affect the quantum well at the LIO/BLSO interface.

In LIO only the deep donors located in the middle of the gap affect the band bending near the interface since the deep acceptors in the middle of the gap will not be ionized near the interface. On the other hand, on the BSO side the deep donors are not ionized while the ionized deep acceptors will affect the band bending near the interface.
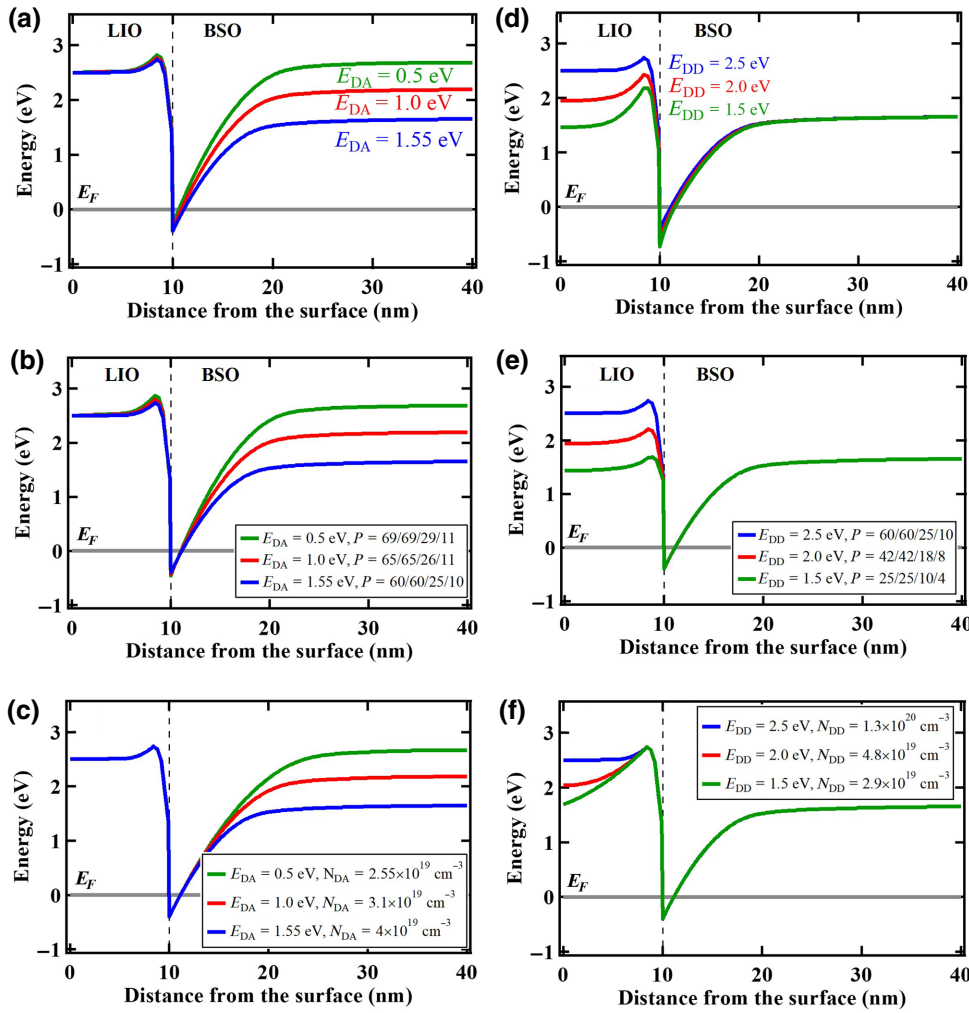
FIG. 5. Influence of the deep-acceptor activation energy of BSO and deep-donor activation energy of LIO on the LIO-undoped BSO interface calculated with the PS equation. (a) Changes in conduction-band bending at different deep-acceptor activation energy of BSO, 0.5, 1.0, and 1.55 eV at LIO 10 nm. (b) Polarization adjustments with other deep-acceptor activation energies of BSO. (c) BSO deep-acceptor density adjustments with other deep-acceptor activation energies of BSO. (d) Changes in conduction-band bending at different deep-donor activation energy of LIO, 1.5, 2.0, and 2.5 eV at LIO 10 nm. (e) Polarization adjustments with other deep-donor activation energies of LIO. (f) LIO deep-donor density adjustments with other deep-donor activation energies of LIO.

The La-dopant level in BSO is higher than its conduction-band minimum, making the La dopants be shallow donors. Therefore, the change of n_{2D} and band bending at different deep acceptor densities and La-donor densities of BSO is investigated. The deep-acceptor density in BSO is reported to be about 4×10^{19} cm^{-3} on MgO substrates [23,40], while it is a little higher, 6×10^{19} cm^{-3}, in BSO on STO substrates [23].

The n_{2D} as a function of LIO thickness with undoped BSO channel and the corresponding conduction-band bending at 10 nm LIO with a deep-acceptor density of 4×10^{19} cm^{-3} of BSO are represented by the purple lines in Figs. 4(a) and 4(b). The green, red, blue, and sky blue lines represent the cases of different deep-acceptor densities in BSO of 1×10^{17} cm^{-3}, 1×10^{18} cm^{-3}, 1×10^{19} cm^{-3}, and 6×10^{19} cm^{-3}.

It is obvious that the n_{2D} of a quantum well is higher with smaller deep-acceptor density, as the less activated acceptor increases the electron carrier density. Furthermore, the slope of the band bending can be easily understood through a simple approximation of the Poisson equation (1), where $\varphi(x)$ is the electric potential, $\rho(x)$

is the charge of the ions and the carriers, and ε is the dielectric constant.

$$\nabla^2 \varphi(x) = -\frac{\rho(x)}{\varepsilon}. \tag{1}$$

The deep acceptors in BSO, the density of which is N_{DA}, will change the electron's potential energy as follows:

$$V(x) = -e\varphi(x) = -\frac{e^2 N_{DA}}{2\varepsilon} x^2 + C_0 x + C_1. \tag{2}$$

Deep acceptor will be the only charge carrier in BSO when the quantum well is made using the undoped BSO channel. The quadratic coefficient is proportional to the deep-acceptor density divided by a dielectric constant, 20 in BSO. The slope of band bending is larger in the case of larger deep-acceptor density and results in the shallower and narrower quantum well, as shown in Fig. 4(b).

The second unique transport property of thermopower measurement in Fig. 2 suggests the very narrow (approximately 1 nm) quantum well, which is mainly related with the large deep-acceptor density in BSO. If we reduce

the deep-acceptor density in BSO with the use of lattice-matched substrate, we get a higher 2DEG carrier density with a wider quantum well, and probably with higher mobility.

As far as the shallow La doping is concerned, the La-doping-dependent electrical properties of the LIO/BLSO interface have previously been reported [12]. Although our main interest will be the 2DEG state formed with undoped BSO, La-doping dependence helps us understand how the quantum wells form. The simulation of the interface is performed with five different La-doping densities ranging from the undoped channel to the 0.4% La-doped channel and they are illustrated in Figs. 4(c) and 4(d). As can be easily imagined, larger La-doping density in BSO produces larger n_{2D} in the interface, as shown in Fig. 4(c), resulting in a deeper and wider quantum well in Fig. 4(d) calculated with a 10-nm LIO layer. In the undoped BSO, the width of the quantum well is only 1.2 nm, whereas in the 0.2% La-doped channel, it is 1.7 nm in Fig. 4(d). As the La-doping density becomes larger than the deep-acceptor density in BSO, in this case starting around 0.3% La doping, the La-doped BSO layer itself will start to lower its conduction band below the Fermi level. In the Poisson equation (1), the La donor has an opposite effect on the band sloping with a positive quadratic coefficient, compared to the effect by the deep acceptors. This is why the band-bending direction changes in the case of 0.4% BLSO 2DEG in Fig. 4(d).

We can now compare the magnitude of n_{2D} with the undoped BSO channel to the second measured transport property, thermopower, in Fig. 2. The n_{2D} of 1.2×10^{13} cm^{-2} from the measurement of thermopower is larger than the n_{2D} value of 1.31×10^{12} cm^{-2} obtained from simulation in Fig. 4(c). However, this difference, especially in the small n_{2D} range (10^{12}–10^{13} cm^{-3}), can originate from a little decrease in the deep-acceptor density in BSO and/or a little increase in the deep-donor density in LIO.

C. Activation energy of the deep-level states

The deep-state levels are considered to be in the center of the band gap; the activation energy of 1.55 eV for the deep acceptors in BSO and 2.5 eV for the deep donors in LIO. However, they might be smaller in reality because most of deep-state activation energies of point defects in perovskite oxides such as LAO, STO, and BSO are between 0.5 eV and half the band gap according to calculations [50–52]. Therefore, it is meaningful to see how adjusting the deep-state activation energy of BSO and LIO will affect the quantum well and its n_{2D}.

First, the deep-acceptor activation energy of BSO is adjusted from 1.55 eV to 1.0 eV and 0.5 eV and what happens to the quantum well at the 10 nm of LIO/undoped BSO interface is investigated. Band bending at a BSO

deep-acceptor activation energy of 0.5, 1.0, and 1.55 eV are indicated by green, red, and blue lines in Fig. 5(a). The slope of the conduction-band bending in BSO increases with lower deep-acceptor activation energy. The Fermi level becomes lower at the surface boundary of the BSO because the lower deep-acceptor level brings down the Fermi level throughout the BSO layer. These change the quantum-well depth. In the case of lower deep-acceptor activation energy of BSO, the higher band slope and the change in the boundary condition of BSO both reduce n_{2D}.

The n_{2D} of the 10 nm LIO/undoped BSO interface is 0 cm^{-2} at 0.5 eV and 4.87×10^{10} cm^{-2} at 1.0 eV of BSO deep-acceptor activation energy. They are less than the n_{2D} of 1.31×10^{12} cm^{-2} in the 10 nm LIO/undoped BSO interface, calculated in Fig. 3 with undoped BSO channel using 1.55 eV deep-acceptor activation energy and the polarization of 60/60/25/10 μC cm^{-2}. If we want to maintain n_{2D} when the deep-acceptor activation energy becomes smaller than 1.55 eV, the polarization value should be increased, as shown in Fig. 5(b). For example, the polarization should increase to 69/69/29/11 μC cm^{-2} at each unit cell of LIO in the case of 0.5 V activation energy and 65/65/26/11 μC cm^{-2} in the case of 1.0 eV. With these adjusted polarizations, n_{2D} is 1.26×10^{12} cm^{-2} at 0.5 eV and 1.30×10^{12} cm^{-2} at 1.0 eV, similar to the value of 1.31×10^{12} cm^{-2} in the case of 1.55 eV activation energy.

Instead of adjusting the polarization we can adjust the deep-acceptor density as the activation energy of the deep-acceptor states varies in order to keep the same n_{2D}. Figure 5(c) shows such cases. As the activation energy decreases to 1.0 eV from 1.55 eV, by changing the acceptor density from 4.0×10^{19} cm^{-3} to 3.1×10^{19} cm^{-3}, we can maintain the same n_{2D}. As activation becomes easier, a smaller density of acceptors is needed. For example, in the case of δ-doped BLSO [53] of a 10 nm 1% doped BSO channel, a deep-acceptor density of 2.5×10^{19} cm^{-3} in BSO with 1.0 eV activation energy generates the same experimental results as a deep-acceptor density of 3.0×10^{19} cm^{-3} with 1.55 eV activation energy does.

The cases for varying LIO deep-donor activation energy are similar. The deep-donor activation energy of LIO is varied from 2.5 eV, which is half of the LIO band gap, to 2.0 and 1.5 eV, and the modified quantum wells are described in Fig. 5(c) with the initial polarizations of 60/60/25/10 μC cm^{-2}. The direction of change is opposite to the effect of the deep-acceptor activation energy of BSO. The band-slope change made by the LIO deep-donor density barely affect the quantum well but more activated deep donors increase the electron carriers and make a deeper quantum well by raising the Fermi level in LIO. This change results in n_{2D} of 1.71×10^{13} cm^{-2} at 2.0 eV and 3.21×10^{13} cm^{-2} at 1.5 eV of the deep-donor activation energy of LIO. To keep the same n_{2D} deduced from the experiments, as we did in Fig. 5(b), polarizations of 42/42/18/8 μC cm^{-2} at 2.0 eV and 25/25/10/4 μC cm^{-2}

at 1.5 eV are needed in Fig. 5(d). Basically smaller polarization is required to compensate for the n_{2D} increase caused by more activated deep donors. The effect on the quantum well by the deep-donor level of LIO is much larger than that by the deep-acceptor level of BSO. In the quantum well that is located below the Fermi level, all BSO deep acceptors are fully activated regardless of deep-acceptor level because they are below the Fermi level in all cases, and the deep-acceptor level mainly affects the band far away from the quantum well and makes little change in 2DEG n_{2D}. On the other hand, the LIO deep-donor level directly affects the quantum-well depth thereby changing the n_{2D} more directly. This is why smaller deep-acceptor activation energy of BSO in Fig. 5(b) requires a smaller increase in polarization while the smaller deep-donor activation energy of LIO in Fig. 5(d) requires a larger decrease in polarization. The combination of smaller BSO deep-acceptor activation energy of 1.0 eV and smaller LIO deep-donor activation energy of 1.5 eV produces n_{2D} of 2.73×10^{13} cm^{-2} with a polarization of 60/60/25/10 μC cm^{-2}. In this case, we need only a polarization of 30/30/11/5 μC cm^{-2} to produce 1.37×10^{12} cm^{-2} of n_{2D}, in line with the experimentally deduced value of 1.31×10^{12} cm^{-2} with 1.55 and 2.5 eV of BSO deep-acceptor and LIO deep-donor activation energies. For comparison, the typical spontaneous polarization of ferroelectric materials are 25–45 μC cm^{-2} in BaTiO$_3$, 40 μC cm^{-2} in KNbO$_3$ and 50–100 μC cm^{-2} PbTiO$_3$ [54].

Same as the deep-acceptor density adjustment in BSO, we can keep the polarization values and adjust the deep-donor density in order to maintain the experimental n_{2D}. Figure 5(f) shows such cases. When the activation energy

of the deep donors in LIO is reduced to 2.0 from 2.5 eV, the necessary deep-donor density for keeping the polarization values and maintaining the experimental n_{2D} is reduced from 1.3×10^{20} cm^{-3} to 4.8×10^{19} cm^{-3}. This is consistent with the idea that the easier it is to activate the donor states, the smaller density of the donors is necessary to have the same effect on the quantum well. Another way to look at this change is by observing the Fermi-level rise in LIO. As the activation energy of the donors decreases, the Fermi level on the LIO side will move up, which creates a larger drop at the interface resulting in larger n_{2D}. This illustrates very well the interplay among the deep-donor density, the activation energy of the deep donors, and the polarization.

D. Effective mass

Figure 6 shows how the effective masses of BSO and LIO affect the quantum well. For our 2DEG state, we are going to assume a triangular quantum well and set the minimum energy of the triangular quantum well to 0. Equation (3) is the nth energy eigenvalue of the triangular quantum well while e is the electron charge, A is the electric field that creates the triangle form of the quantum well, the same as the slope of the conduction band in the LIO/BLSO case, $\hbar$ is the Plank constant, m is the effective mass, and a_n is the nth zero of the Airy function, which has a minus value.

$$E_n = -\left(\frac{e^2 A^2 \hbar^2}{2m} \right)^{1/3} a_n. \tag{3}$$

Figures 6(a) and 6(b) show the n_{2D} of 2DEG according to LIO thickness and band bending with 10 nm LIO
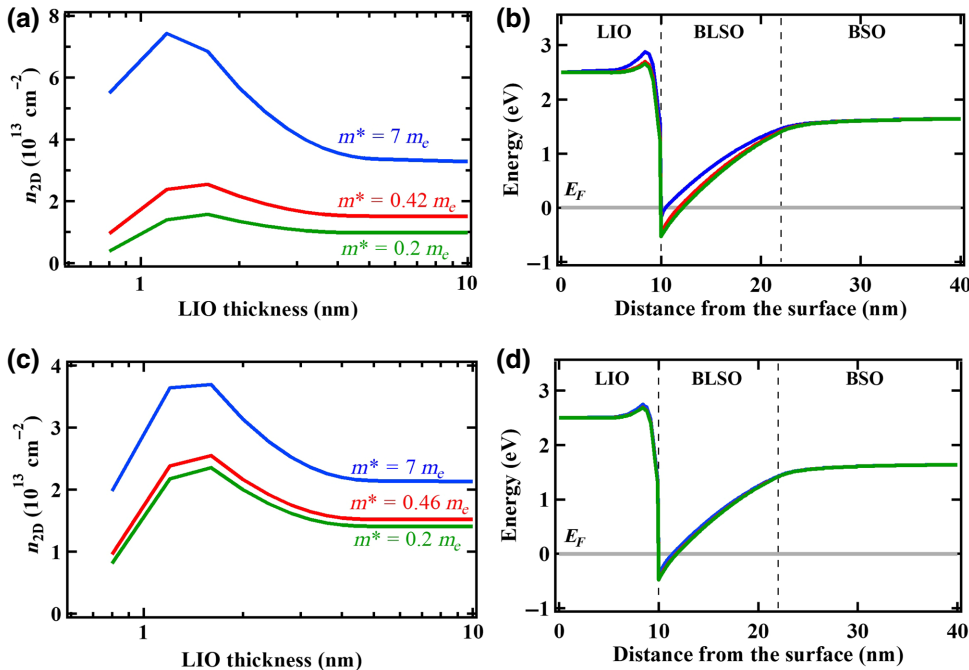
FIG. 6. Influence of the effective masses of BSO and LIO on the LIO-BLSO interface. (a) n_{2D} of the quantum well with BSO effective masses of 0.2, 0.42, and 7 m_e as a function of the LIO thickness. (b) Changes in conduction-band bending at each effective mass of BSO at LIO 10 nm. (c) n_{2D} of the quantum well with LIO effective masses of 0.2, 0.46, and 7 m_e as a function of the LIO thickness. (d) Changes in conduction-band bending at each effective mass of LIO at LIO 10 nm.

of 2DEG at 0.2 m_e, 0.42 m_e, and 7 m_e of BSO effective mass while the experimentally measured effective mass of BSO is around 0.42 m_e [46]. The n_{2D} is much greater in the case of the effective mass of 7 m_e, indicated by the blue line, than those of smaller effective masses, although the quantum well is shallower and narrower at larger effective mass. This is possible by the relationship between the density of state and the effective mass in each bound state energy. In the 2D state, the density of state is proportional to the effective mass while it is also proportional to the energy value that is inversely proportional to the 1/3 power of effective mass in Eq. (3). However, the n_{2D} difference is slightly smaller than the value of effective mass to the 2/3 because there are small differences in A in the three cases. Overall, as the effective mass increases, the density of state increases, which can create high n_{2D} even in a shallow and narrow quantum well. In the case of BSO, not too small an effective mass of 0.42 m_e bodes well for the high n_{2D}.

Since the 2DEG quantum well is on the BSO side, it can be thought that the effective mass of LIO should not affect the n_{2D} of 2DEG. However, the effective mass of LIO also affects n_{2D} showing an increase at higher effective mass, and this is because the 2DEG quantum well is not located entirely on the BSO side. The electron carriers also span a LIO of about 1 nm from the interface when it is calculated with 0.46 m_e of LIO effective mass in Fig. 6(d), which has a 3D carrier density of 1.53×10^{15} cm^{-3} in the LIO of 1 nm away from the interface. Naturally, the effect of the LIO effective mass is much smaller than that of the BSO effective mass. There is only a small change in the band bending, shown in Fig. 6(d), and the effect on the density of state is also small in Fig. 6(c). From these analyses, it

can be presumed that the large effective masses of BSO and LIO compared to other conventional semiconductors for 2DEG, are conducive to creating higher density 2DEG.

E. Dielectric constant

The dielectric constant also plays a role in forming 2DEG. In Fig. 7(a), n_{2D} is plotted as a function of the LIO thickness in cases of four different dielectric constants of BSO, 10, 20, 50, and 100, where 20 is the experimentally obtained value [46]. When the dielectric constant goes up, n_{2D} goes down making the shallow quantum well in Fig. 7(b) roughly. As can be seen from Eqs. (1) and (2), the band-bending slope is inversely proportional to the dielectric constant while it is proportional to the ionized carrier density, and the role of dielectric constants in BSO and LIO can be understood in the same way as for the LIO deep-donor density and the BSO deep-acceptor density. The absolute value of the quadratic coefficient of the band slope of BLSO decreases in Fig. 7(b) as the dielectric constant of BSO increases. This makes a shallower and wider quantum well with the smallest n_{2D} of the purple line at the largest BSO dielectric constant value of 100. Overall, the smaller dielectric constant in BSO generates a deeper and narrower quantum well. While deeper quantum wells generate higher n_{2D}, narrower quantum wells generate lower n_{2D}. This is why in Fig. 7(a) the n_{2D} value is not a monotonic function of the dielectric constant of BSO.

The changes in n_{2D} and band-bending slope as the dielectric constant of LIO varies are the same as that of changes due to the BSO dielectric constant variation. When the dielectric constant of LIO rises from 25 to 38
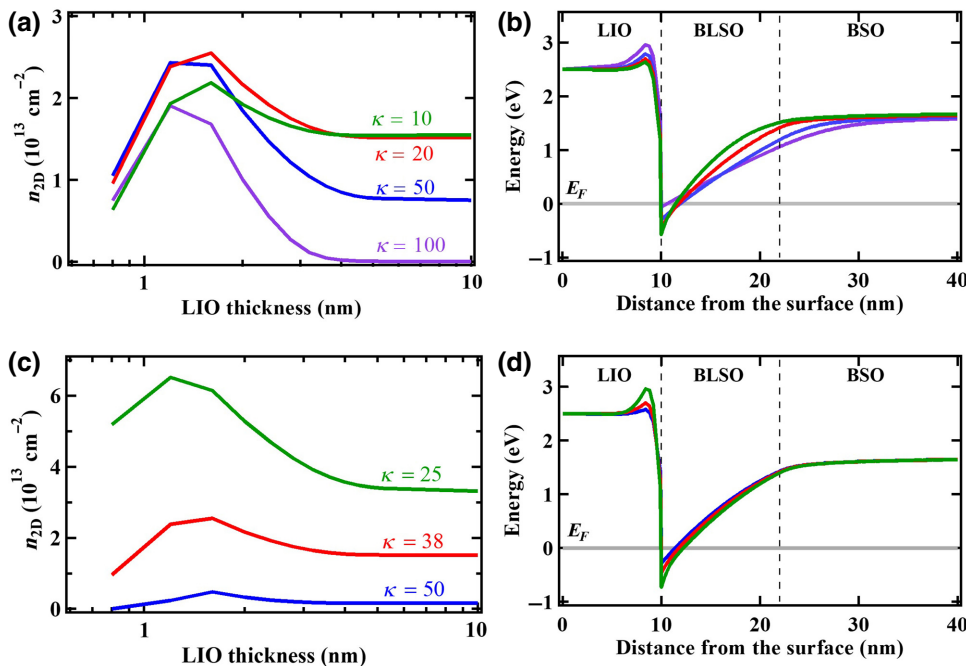
FIG. 7. Influence of the dielectric constant of BSO and LIO on the LIO-BLSO. (a) n_{2D} of the quantum well with BSO dielectric constants of 10, 20, 50, and 100 as a function of the LIO thickness. (b) Changes in conduction-band bending at each dielectric constant of BSO at LIO 10 nm. (c) n_{2D} of the quantum well with LIO dielectric constants of 25, 38, and 50 as a function of the LIO thickness. (d) Changes in conduction-band bending at each dielectric constant of LIO at LIO 10 nm.
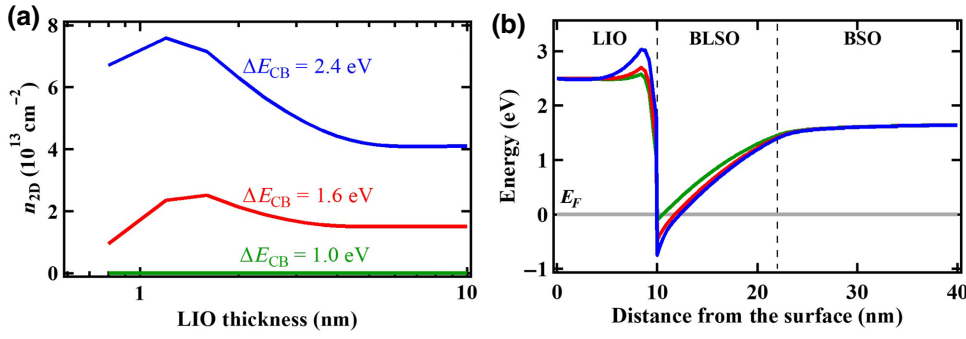
FIG. 8. Influence of the conduction-band offset between BSO and LIO on the LIO-BLSO interface. (a) n_{2D} of the quantum well with conduction-band offsets of 1.0, 1.6, and 2.4 eV as a function of the LIO thickness. (b) Changes in conduction-band bending at each conduction-band offset at LIO 10 nm.

and 50, n_{2D} goes down in Fig. 7(c), making a shallower quantum well at the interface with lower band-bending slope in Fig. 7(d). In addition, we can see one more phenomenon caused by a change in the dielectric constants. There is a high electric field at the interface in the case of the LIO dielectric constant of 25, represented by the green line in Fig. 7(d), even though the dielectric constant of LIO barely affects the band slope near the quantum well where polarization exists, as can be seen in the role of deep donors in Fig. 3(d). The change in the electric field at the interface is because the dielectric constant is related with the electric field created by polarization. As the dielectric constant decreases, the electric field of the same polarization increases because the electric field is proportional to the polarization and inversely proportional to the dielectric constant. Small dielectric constant requires large polarization to create the same electric field. In fact, this is the main reason for generating higher n_{2D} with lower dielectric constant and the n_{2D} in Fig. 7(c) is also larger than the n_{2D} in Fig. 7(a) with a similar value of dielectric constant. The first transport property of high n_{2D} is not interfered by the LIO dielectric constant because it is not too large, enabling not too shallow a quantum well. The dielectric constant plays a larger role in the formation of the 2D interface of LIO/BLSO than other material parameters because the dielectric constant varies over a large range compared to other parameters that vary only in a small range depending on materials and/or temperatures. For example, the electron effective mass differs by about less than 10 times for

each material. However, it is known that the dielectric constant of STO increases to 18 000 at low temperature [55] while the dielectric constants of BSO and LIO hardly change with the temperature [56,57]. Having an appropriate value for the dielectric constant is necessary. Larger dielectric constant produces wider and shallower quantum wells by reducing the band-bending slope, eventually resulting in loss of 2D characteristics.

F. Conduction-band offset

The conduction-band offset between LIO and BSO makes an electric field at the interface with the help of polarization, playing the same role as the interface polarization already shown in Fig. 3(b). In Figs. 8(a) and 8(b), three kinds of conduction-band offset 1.0, 1.6, and 2.4 eV are described. The higher conduction-band offset makes a higher electric field and a higher slope of the energy band at the interface in Fig. 8(b), resulting in a higher n_{2D} in Fig. 8(a). Larger conduction-band offset compared to the conventional 2DEGs is mainly responsible for the first transport property of high n_{2D} at the LIO/BSO interface. In Fig. 8(a), a conduction-band offset of 2.4 eV in the blue line generates the carrier density n_{2D} even larger than 4×10^{13} cm^{-2} with a 0.2% La-doped channel and 10-nm LIO. However, when the conduction-band offset goes down to 1.0 eV, indicated by the green line, there is no quantum well forming below the Fermi level in Fig. 8(b), resulting in no 2D carrier density. To form a 2DEG on

TABLE II. Material parameters used for GaAs, AlGaAs, GaN, AlGaN, ZnO, and MgZnO.

	GaAs	Al$_{0.32}$Ga$_{0.68}$As	GaN	Al$_{0.32}$Ga$_{0.68}$N	ZnO	Mg$_{0.32}$Zn$_{0.68}$O
m_e^*/m_0	0.067	0.096	0.27	0.37	0.30	0.49
κ	13.1	11.1	10.4	9.54	8.10	8.68
E_g (eV)	1.42	1.82	3.44	4.19	3.35	4.10
ΔE_C (eV)	−	0.35	−	1.1	−	0.59
PSP (μC cm^{-2})	0	0	2.90	4.56	5.40	7.43
P_{PE} (μC cm^{-2})	0	$<1 \times 10^{-3}$	0	1.17	0	1.10
N_{DD} (cm^{-3})	1×10^{16}	1×10^{17}	1×10^{15}	1×10^{15}	1×10^{16}	1×10^{16}
E_{DD} (eV)	0.44	0.05	0.53	0.53	0.3	0.3
N_{DA} (cm^{-3})	1×10^{16}	1×10^{16}	1×10^{17}	1×10^{17}	1×10^{15}	1×10^{15}
E_{DA} (eV)	0.38	0.38	1.2	1.2	0.2	0.2
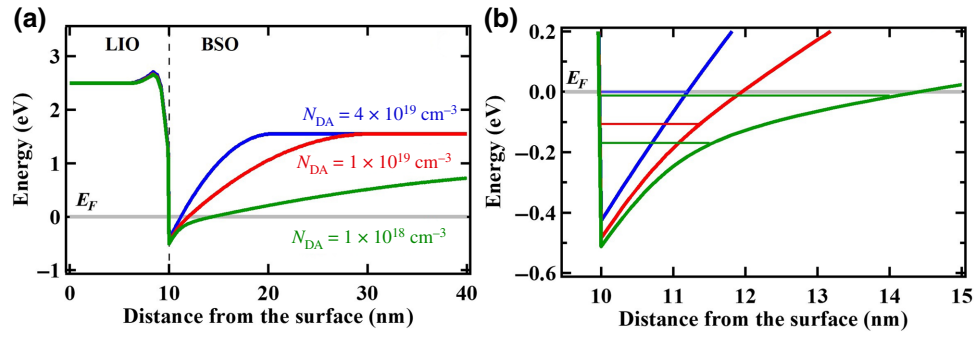
FIG. 9. Influence of reduced deep-acceptor density of BSO on the LIO-undoped BSO interface calculated with the PS equation at a temperature of 4 K. (a) Conduction-band bending of the interface with 1×10^{18} cm^{-3}, 1×10^{19} cm^{-3}, and 4×10^{19} cm^{-3} deep-acceptor density. (b) Enlarged views of the conduction band near the interface with sub-band energies of the 2D quantum wells at each of the deep-acceptor densities of BSO.

the LIO/BLSO interface, a conduction-band offset of more than 1.0 eV is required. Fortunately, the conduction-band offset between LIO and BSO is measured to be 1.6 eV by a tunneling experiment [49] and theoretically predicted to be larger than 2.06 eV [39]. This value is much greater than 1.0 eV and is at the same time much larger than the conduction-band offset of other conventional 2DEGs, as shown in Table II. The conduction-band offsets of the GaAs, GaN, ZnO interface are 0.35, 1.1, and 0.59 eV. These small values are because the alloyed heterostructures are used to make the conventional 2DEGs, usually possessing a smaller difference in the conduction-band offset that the nonalloyed cases. In LIO/BLSO 2DEG, two completely different materials are combined to make the interface, and the large conduction-band offset is advantageous for making the high-density 2DEG.

IV. DISCUSSIONS

We investigate the roles of several material parameters of LIO and BSO in formation of 2DEG at the interface and show that reasonable material parameters can form the 2DEG with two distinct properties: high carrier density in a narrow quantum well. First, the polarization, though it is located only near the interface, is large enough to form a deep quantum well by generating large

electric field at the interface. Second, the deep-state densities seem in an appropriate range; the acceptor density in BSO is not too large to trap the entire electronic carriers in the channel and the deep-donor density in LIO is large enough to screen the interface polarization. Third, the intentional and shallow La donor of BSO can adjust the quantum-well depth. Fourth, LIO and BSO possess not too small effective masses, not too large dielectric constants, and large enough conduction-band offset, necessary for high n_{2D}.

While most material parameters of LIO and BSO cannot be changed, if we find a way to reduce the threading dislocation density of the BSO film, the deep-acceptor density in BSO can be reduced. We can reduce the deep-acceptor density by using homoepitaxial substrates of BSO [58] or such substrates as Ba_2ScNbO_6, and LIO that have almost the same lattice constants with the BSO channel layer [59,60]. We investigate how LIO/BSO 2DEGs will change when we reduce the deep-acceptor density this way, focusing on the sub-band levels, similar to the calculations we have already done in Figs. 4(a) and 4(b) at the temperature of 300 K. Here, we calculate at the temperature of 4 K to see the energy eigenvalues clearly and compare them with the results of Figs. 10–12 of the conventional 2DEGs. In the blue line in Fig. 9(a), the conduction band that forms the 2DEG is plotted in the case of undoped BSO, including the deep-acceptor density of 4×10^{19} cm^{-3}

(a)
Schottky barrier = 0.15 eV

Si-doped $Al_{0.32}Ga_{0.68}$As 30 nm
$N_{DD} = 1 \times 10^{17}$ cm^{-3} ($E_a = 0.05$ eV)
$N_{DA} = 1 \times 10^{16}$ cm^{-3} ($E_a = 0.38$ eV)

GaAs 500 nm
$N_{DD} = 1 \times 10^{16}$ cm^{-3} ($E_a = 0.44$ eV)
$N_{DA} = 1 \times 10^{16}$ cm^{-3} ($E_a = 0.38$ eV)

Slope = 0
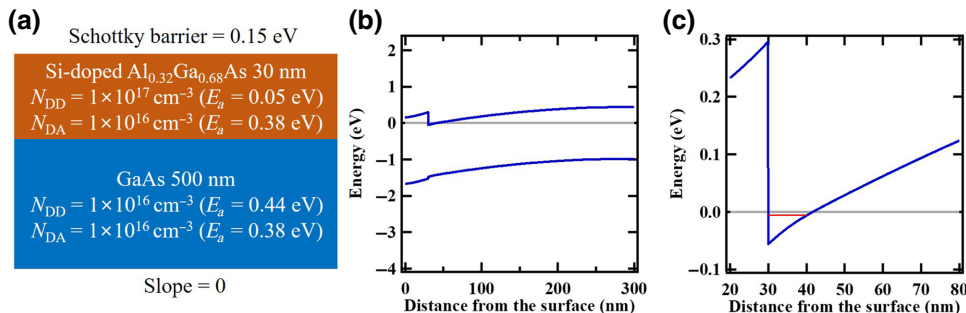
FIG. 10. PS simulation of (AlGa)As/GaAs 2DEG. (a) Structure and parameters for calculation. (b) Calculation result of conduction-band energy for the Fermi level of 0 eV. (c) An enlarged view of (b) near the interface of (AlGa)As and GaAs with a sub-band energy of the red line.
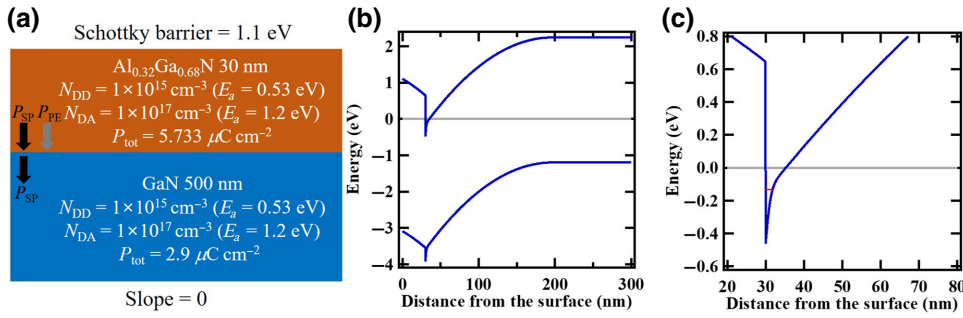
FIG. 11. PS simulation of (AlGa)N/GaN 2DEG. (a) Structure and parameters including the direction of the polarizations for calculation. (b) Calculation result of conduction-band energy for the Fermi level of 0 eV. (c) An enlarged view of (b) near the interface of (AlGa)N and GaN with a sub-band energy of the red line.

obtained from experimental electrical properties under optimal growth conditions [12,23]. The cases for a reduced deep-acceptor density of 1×10^{19} and 1×10^{18} cm^{-3} are also presented, which show a deeper and wider quantum well indicated by the red and green lines. They have n_{2D} of 8.89×10^{10} cm^{-2} in the blue line, 1.87×10^{13} cm^{-3} in the red line, and 3.19×10^{13} cm^{-3} in the green line. In Fig. 9(b), the energy and length scales are enlarged and the sub-bands for each deep-acceptor density are presented. The sub-bands are -0.0004 eV at a deep-acceptor density of 4×10^{19} cm^{-3}, -0.1063 eV at 1×10^{19} cm^{-3}, and -0.0123 eV and -0.1693 eV at 1×10^{18} cm^{-3} with an undoped BSO channel. The quantum well becomes deeper and wider with lower deep-acceptor density, creates higher energies of electrons, and makes a high-density 2DEG state. In the case of an undoped BSO channel layer and a 10-nm LIO when the BSO deep-acceptor density is 4×10^{19} cm^{-3}, a quantum well with a depth of 0.43 eV and a width of 1.1 nm forms, as in the blue line of Fig. 5. At a BSO deep-acceptor density of 1×10^{18} cm^{-3}, it has over 3×10^{13} cm^{-3} of n_{2D} at 10-nm LIO and over 4×10^{13} cm^{-3} of n_{2D} at 4 unit cells of LIO, even using the channel without La doping at temperature of 4 K. Using such an undoped BSO channel will help avoid ionized impurity scattering in the channel. Now with reducing the deep-acceptor density of BSO, the n_{2D} of 2DEG will be much larger than that of conventional 2DEGs, which would be a great advantage of LIO/BSO 2DEG.

We can list five big differences between the LIO/BSO interface and conventional 2DEGs. First, in the LIO/BSO, the electric field at the interface made by polarization and

conduction-band offset is much larger than that of the conventional 2DEGs. The detailed values of the conduction-band offsets and the polarizations are available in Tables I and II in the following Appendix. In Figs. 10–12 in the Appendix, the three types of 2DEGs have a quantum well with a depth of 0.05–0.46 eV and width of 5–12 nm. The resulting deeper quantum well helps the formation of high n_{2D} in the LIO/BSO interface. Second, the quantum-well width is very narrow compared to conventional 2DEGs, experimentally confirmed in Fig. 2. This is mainly related to the large deep-acceptor density of BSO. However, despite the narrow width of the quantum well, it makes a large n_{2D} due to the deep quantum well. However, as we reduce the deep-acceptor density in BSO in order to increase the mobility, the width of the quantum well is expected to increase. Third, there is no band slope on the LIO end surface while three conventional 2DEGs have an electric field at the surface boundary of the alloyed layers. For the GaAs case, the slope occurs from the pinned Fermi level of the surface, which is made by surface deep states. The band slope in the cases of the GaN and ZnO is due to the constant polarization across the entire alloyed layer in addition to pinned Fermi levels. In contrast, the LIO has polarization and electric field only near the interface because all polarization charges are screened by the large density of ionized deep donors and the band becomes flat before the LIO end surface. Above a certain thickness of LIO, we can see the flat band near the surface from the previous calculation results. Even if we set the boundary condition of the LIO to have Fermi-level pinning like the conventional 2DEGs, lowering the deep-state
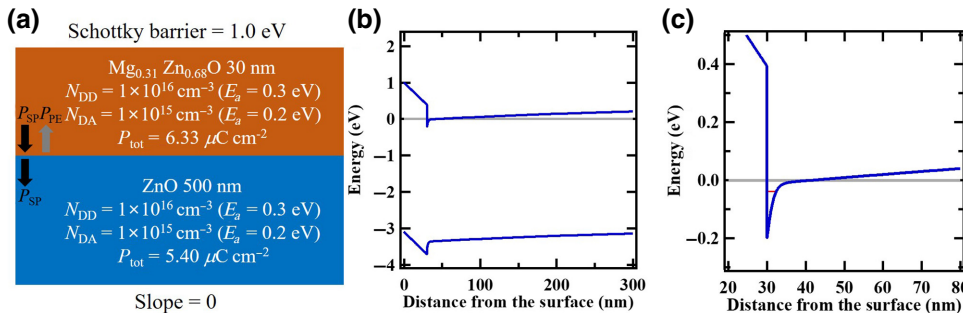
FIG. 12. PS simulation of (MgZn)O/ZnO 2DEG. (a) Structure and parameters including the direction of the polarizations for calculation. (b) Calculation result of conduction-band energy for the Fermi level of 0 eV. (c) An enlarged view of (b) near the interface of (MgZn)O and ZnO with a sub-band energy of the red line.

activation energy like in Figs. 5(d)–5(f), large-density deep donors can still flatten all the conduction-band slope. However, relatively small amounts of deep carriers of (AlGa)N and (MgZn)O cannot sufficiently screen the space charges from polarization and therefore can maintain the electric field at the surface. Fourth, there is a possibility of large Rashba effect at the LIO/BLSO interface created by large spin-orbit coupling because there is large electric field at the interface, and LIO and BSO have higher atomic masses compared to previous semiconducting materials that form 2DEGs. If there is Rashba effect at the interface, the high-energy eigenvalue and high n_{2D} can be used in spintronics, separating electrons to spin up and spin down clearly. Fifth, the perovskite structure of LIO and BSO can be combined with other perovskite materials that have interesting properties such as ferroelectrics. This combination may make it possible to pioneer fields that have not been studied so far. Many perovskite oxide materials with a large band gap and a high dielectric constant including LIO will be able to modulate the high carrier density of LIO/BLSO 2DEG [12].

V. CONCLUSIONS

We experimentally obtain two special transport properties different from conventional 2DEGs: large n_{2D} (2–3×10^{13} cm^{-2}) and a narrow (approximately 1 nm) quantum well. By using PS simulation we show that these properties can be explained well with reasonable material parameters basically in a semiconductor picture with a unique "interface polarization." We investigate the roles the 13 material parameters play in forming the quantum well. We first set two unknown parameters, polarization and deep-donor density of LIO to fit the experimental results and investigate the changes that the two values can bring about. Next, the effects of changing donor density and deep-acceptor density of BSO, deep-state activation energy, effective mass, dielectric constant, and conduction-band offset are studied and qualitatively understood with the aid of the simplistic Poisson-Schrödinger equation. Through these analyses, we realize the uniqueness of the LIO and BSO material parameters for forming a quantum well with high n_{2D} and narrow width. We also show what changes further development of the LIO/BLSO interface in reducing the deep-acceptor density of BSO will bring about. The attempt to analyze the influence of the material parameters on perovskite oxide heterostructures in this paper will help to study the physical properties of 2D quantum wells and their applications. The unique properties of large n_{2D} and the narrow width of the 2DEG at the LIO/BSO interface will be very useful in enhancing the current and power-handling capabilities of HEMT devices. Combined with its excellent chemical stability, high mobility at room temperature, and large band gap,

the BSO-based heterostructures show a large potential for high-power, high-speed transparent electronics.

APPENDIX: PS SIMULATIONS OF CONVENTIONAL 2DEGs

In this Appendix, we confirm that the calculation tool used in our PS simulations effectively describe the experimental results obtained to date for conventional 2DEGs. $(Al_{0.32}Ga_{0.68})As/GaAs$, $(Al_{0.32}Ga_{0.68})N/GaN$, and $(Mg_{0.32}Zn_{0.68})O/ZnO$ are simulated with the available material parameters at room temperature. Effective masses, dielectric constants, band gaps, conduction-band offsets, and polarizations of GaAs [61,62], $(Al_{0.32}Ga_{0.68})As$ [61,62], GaN [3,62,63], $(Al_{0.32}Ga_{0.68})N$ [3,63–66], ZnO [62,67–69], and $(Mg_{0.32}Zn_{0.68})O$ [67–71] are listed in Table II. The densities and activation energy of the donors and the acceptors are obtained through other experiments or calculations [72–80]. However, since the parameters for the donors and the acceptors are known only as ranges of values and are not very critical for calculation results, we enter some values in the known ranges.

For the boundary conditions, the "Schottky" boundary condition is applied because the surface of alloyed larger band-gap materials have a Fermi-level pinning determined by the surface deep states [73,81,82]. On the other hand, the "slope = 0" boundary condition that the band slope goes to zero is placed on the surface boundary of the thick nonalloyed substrate. Even if there is a Fermi-level pinning at the end boundary of the substrate, it is not considered here for simplicity, since it does not affect the quantum well as the large substrate thickness cancels out the effect of the surface boundary. Using nine kinds of material parameters, excluding shallow carriers that we did not consider here, and the boundary conditions, we calculate the band bending at the GaAs, GaN, and ZnO interfaces with 30-nm-alloyed larger band-gap film over the 500 nm of nonalloyed smaller band-gap substrate with 32% of the alloying ratio. Although we use material parameters at room temperature, calculations are done at 4 K to clearly see the sub-band energies since the calculation results at room temperature are not very different.

1. (AlGa)As/GaAs 2DEG

First, the GaAs interface, which is the simplest 2DEG, is simulated with the structure shown in Fig. 10(a). The boundary conditions, concentrations of acceptor and donor with activation energies, and polarization values and directions are also described in Fig. 10(a). The Si dopant in

(AlGa)As is considered as a deep-donor state with 0.05-eV activation energy. The unknown values of (AlGa)As, namely the concentration and the activation energy of deep acceptors, are set to be the same values as in GaAs. (AlGa)As and GaAs have a zinc-blende structure, which is of a hexagonal symmetry. This structure has an inversion symmetry breaking that can make spontaneous polarization in the bulk of (AlGa)As and GaAs, and the strain gradient at the interface can make piezoelectric polarization in (AlGa)As. However, the spontaneous polarization of (AlGa)As and GaAs is known to be almost zero, and the piezoelectric polarization of (AlGa)As is known to be negligible, as shown in Table II. Therefore, formation of GaAs 2DEG is explained by a "modulation-doping" model in which the 2DEG interface is created mainly by the conduction-band offset [14].

The conduction-band-bending result of the simulation is plotted with blue lines in Fig. 10(b) relative to the Fermi level located at 0 eV, and Fig. 10(c) is the enlarged conduction-band minimum of the interface with the bound-state energy eigenvalues indicated by a red line. A quantum well is formed at the interface, and the result is consistent with the experimental results mentioned above. In Figs. 10(b) and 10(c), it shows a quantum well of 11.6-nm width where the conduction-band minimum locates below the Fermi level. The interface quantum well has an n_{2D} of 1.68×10^{11} cm^{-2}, which is close to about 1×10^{11} cm^{-2} in GaAs interfaces, found in experiments [5,8]. The bound-state energy described in Fig. 10(c) is -0.0060 eV for (AlGa)As/GaAs. We can confirm that our simulation method is valid, using the "Schottky" boundary condition of 0.15 eV at the surface in Fig. 10(b) and "slope = 0" boundary condition that change the conduction-band slope to zero as the x-axis value increases. In agreement with the "modulation-doping" model, the conduction-band offset at the interface creates the quantum well below the Fermi level by lowering the conduction band at the interface.

2. (AlGa)N/GaN 2DEG

Second, we simulate the GaN interface. The boundary conditions, the acceptor, and the donor densities with their activation energies, the polarization values and their directions are described in Fig. 11(a) along with the structure used for simulation. There is no intentional dopant and some unknown values of (AlGa)N, such as the concentrations and the activation energies of deep carriers, are set to be the same values as in GaN. GaN and (AlGa)N have a wurtzite structure classified as a hexagonal structure, and the inversion symmetry is broken, enabling spontaneous polarization shown in Table II and piezoelectric polarization that is caused by the strain in (AlGa)N. The conduction-band offset and the polarization discontinuity at the interface are known to be the main causes for 2DEG

formation, which is often referred to as "polarization doping" [3].

The band-bending results of our simulation are plotted in Fig. 11(b), and Fig. 11(c) is a magnified view near the interface with the bound-state energy eigenvalue as the red line. A deep quantum well exists at the interface, which is also consistent with the previously mentioned experimental results. Figures 11(b) and 11(c) depict a quantum well of 5.2 nm width and 1.51×10^{13} cm^{-2} n_{2D}, which is close to about 1×10^{13} cm^{-2} of the GaN interface in the experiments [3,6]. The bound-state energy in Fig. 11(c) is -0.1323 eV. We use the "Schottky" boundary condition of 1.1 eV at the surface in Fig. 11(b) and "slope = 0" boundary condition at the bottom of the structure. As the "polarization-doping" model suggests, the polarization discontinuity at the interface along with the conduction-band offset at the interface enables a quantum well with the downward slope in (AlGa)N.

The conduction-band slope is mainly determined by the polarization, the dielectric constant, the density and the energy levels of deep-level dopants, the boundary conditions, and the conduction-band offset. In (AlGa)N, the slope of the conduction band can be obtained by the charge neutrality condition that contains all these parameters [83]. This slope becomes smaller with increasing thickness of (AlGa)N, explaining the 2DEG density that becomes saturated experimentally with increasing (AlGa)N thickness [17,18]. The slope of GaN must also consider all these parameters, but it can be simply understood as the deep-carrier activation and the polarization. They affect each other and eventually the band bending near the interface. The polarization discontinuity near the interface lowers the conduction band, generates a quantum well below the Fermi level, and prevents activation of the deep donors in GaN, whereas the deep acceptors are all activated because they are located far below the Fermi level. As the x-axis value increases in GaN, the conduction band rises upward under the influence of the activated deep acceptors, and the deep donors start to be activated as their energy level goes above the Fermi level, which changes the slope to zero. When this happens, the polarization of GaN is invisible because it is canceled out by the deep carriers. Once the slope of the band disappears, charge neutrality remains with the flat band until the end of the GaN.

3. (MgZn)O/ZnO 2DEG

Third, the ZnO interface is simulated. The parameters for the calculation and the structure of the interface are described in Fig. 12(a). There is no intentional dopant and some unknown values of (MgZn)O, such as the concentrations and the activation energies of deep carriers, are set to the same values as in ZnO. (MgZn)O and ZnO have the same wurtzite structure as GaN, with the broken inversion symmetry. Large spontaneous polarization

exists in each material, shown in Table II with a similar piezoelectric polarization value of (MgZn)O as that of (AlGa)N. However, the direction of piezoelectric polarization of (MgZn)O grown epitaxially on ZnO is in the opposite direction of the spontaneous polarization of GaN and (AlGa)N, reducing the total magnitude of the polarization discontinuity. Here, alloyed (MgZn)O is placed on top for the consistency with GaAs and GaN 2DEG cases. However, the (MgZn)O are usually placed at the bottom for larger carrier-density 2DEG, since in such a case the direction of the piezoelectric polarization in ZnO coincides with the direction of spontaneous polarization in ZnO, which enhances the effect of the polarization discontinuity at the interface. The same as the GaN interface, the polarization discontinuity and the conduction-band offset at the interface are known to be the main causes of ZnO 2DEG formation, which is referred to as "polarization doping" [4].

The band-bending results obtained through simulations are plotted in Fig. 12(b), and Fig. 12(c) is an enlarged view of the conduction-band minimum near the interface with bound-state energy eigenvalues. Figures 12(b) and 12(c) show a quantum well with a width of 11.4 nm and n_{2D} of 4.80×10^{12} cm^{-2}, which is slightly smaller than the experiment results [4,7] of about 1×10^{13} cm^{-2} due to the swapped positions of (MgZn)O and ZnO. The bound-state energies described in Fig. 12(c) is -0.0377 eV. We also use the same boundary conditions, though there seems to be a sloped band at the ZnO bottom because the bottom side of the graph is cut off in the figure. The same as the GaN interface, it is shown that the conduction-band offset and the polarization discontinuity together produce band bending and the resulting quantum well.

4. Comparison of three conventional 2DEGs

Our calculations reveal that the main parameters that make big differences among the three 2DEGs are the conduction-band offset, the polarization, and/or the effective mass because these values show a big difference. In (AlGa)N/GaN, we can see the deepest quantum well when comparing Figs. 10(b), 11(b), and 12(b) described in the same scale, and the largest bound-state energy level can be seen when comparing Figs. 10(c), 11(c), and 12(c). This results from the largest conduction-band offset and the largest polarization discontinuity in the GaN interface, which plays a crucial role in creating the biggest conduction-band discontinuity at the interface of 1.1 eV when it is only 0.35 eV at GaAs and 0.59 eV at the ZnO interface. The polarization discontinuity between the two materials at the GaN interface is also biggest with 2.833 μC cm^{-2} while they are about 0 μC cm^{-2} at the GaAs interface, and 0.93 μC cm^{-2} at the ZnO interface. In addition to the effect of smaller conduction-band offset and polarization discontinuity, the smaller n_{2D} of the

GaAs interface is also due to the smaller effective mass of GaAs than GaN and ZnO. The density of state of a 2D quantum well is proportional to the absolute value of the bound-state energy (E_F–E), and it is also proportional to the effective mass. This is why the n_{2D} of the GaAs interface is more than 10 times smaller than that of the ZnO interface, although the absolute value of the bound-state energy level of the GaAs interface is about 1/6 of that of the ZnO interface.

The calculated values of n_{2D} can vary with the change in the density and activation energy of the donor and the acceptors as well as the boundary conditions that are different at each material for three types of 2DEGs, and there is a large variation in the experimental reference values. However, they do not change the characteristics of the quantum well very much because the most relevant parameters for quantum-well formation are the conduction-band offset and the polarization value in 2DEGs. For example, when the deep-acceptor activation energies of (AlGa)N and GaN in (AlGa)N/GaN are changed from 1.2 to 0.5 eV, n_{2D} changes from 1.51×10^{13} cm^{-2} to 1.49×10^{13} cm^{-2}, and when the Schottky boundary condition on the (AlGa)N surface in (AlGa)N/GaN changes from 1.1 to 0.1 eV, the n_{2D} changes from 1.51×10^{13} cm^{-2} to 1.68×10^{13} cm^{-2}, which are not significant differences. In the same sense, we do not need to worry too much about the accuracy of these parameters because the existence of a quantum well is solid, and the order of magnitude for the 2DEG carrier density is reliable.

[1] T. Mimura, Development of high electron mobility transistor, Jpn. J. Appl. Phys. **44**, 8263 (2005).

[2] J. A. Simmons, H. P. Wei, L. W. Engel, D. C. Tsui, and M. Shayegan, Resistance Fluctuations in Narrow AlGaAs/GaAs Heterostructures: Direct Evidence of Fractional Charge in the Fractional Quantslsss Hall Effect, Phys. Rev. Lett. **63**, 1731 (1989).

[3] O. Ambacher, J. Smart, J. R. Shealy, N. G. Weimann, K. Chu, M. Murphy, W. J. Schaff, L. F. Eastman, R. Dimitrov, L. Wittmer, M. Stutzmann, W. Rieger, and J. Hilsenbeck, Two-dimensional electron gases induced by spontaneous and piezoelectric polarization charges in N- and Ga-face AlGaN/GaN heterostructures, J. Appl. Phys. **85**, 3222 (1999).

[4] H. Tampo, H. Shibata, K. Matsubara, A. Yamada, P. Fons, S. Niki, M. Yamagata, and H. Kanie, Two-dimensional electron gas in Zn polar ZnMgO/ZnO heterostructures grown by radical source molecular beam epitaxy, Appl. Phys. Lett. **89**, 132113 (2006).

[5] L. Pfeiffer, K. W. West, H. L. Stormer, and K. W. Baldwin, Electron mobilities exceeding 10^7 cm²/Vs in modulation-doped GaAs, Appl. Phys. Lett. **55**, 1888 (1989).

[6] M. J. Manfra, L. N. Pfeiffer, K. W. West, H. L. Stormer, K. W. Baldwin, J. W. P. Hsu, D. V. Lang, and R. J. Molnar, High-mobility AlGaN/GaN heterostructures grown by

molecular-beam epitaxy on GaN templates prepared by hydride vapor phase epitaxy, Appl. Phys. Lett. **77,** 2888 (2000).

[7] A. Tsukazaki, H. Yuji, S. Akasaka, K. Tamura, K. Nakahara, T. Tanabe, H. Takasu, A. Ohtomo, and M. Kawasaki, High electron mobility exceeding 10^4 cm^2 V^{-1} s^{-1} in Mg$_x$Zn$_{1-x}$O/ZnO single heterostructures grown by molecular beam epitaxy, Appl. Phys. Express **1,** 055004 (2008).

[8] Z. Schlesinger, W. I. Wang, and A. H. MacDonald, Dynamical Conductivity of the GaAs Two-Dimensional Electron Gas at Low Temperature and Carrier Density, Phys. Rev. Lett. **58,** 73 (1987).

[9] G. Herranz, F. Sánchez, N. Dix, M. Scigaj, and J. Fontcuberta, High mobility conduction at (110) and (111) LaAlO$_3$/SrTiO$_3$ interfaces, Sci. Rep. **2,** 758 (2012).

[10] S. Thiel, G. Hammerl, A. Schmehl, C. W. Schneider, and J. Mannhart, Tunable quasi–Two-dimensional electron gases in oxide heterostructures, Science **313,** 1942 (2006).

[11] U. Kim, C. Park, Y. M. Kim, J. Shin, and K. Char, Conducting interface states at LaInO$_3$/BaSnO$_3$ polar interface controlled by Fermi level, APL Mater. **4,** 071102 (2016).

[12] Y. Kim, Y. M. Kim, J. Shin, and K. Char, LaInO$_3$/BaSnO$_3$ polar interface on MgO substrates, APL Mater. **6,** 096104 (2018).

[13] D. Song, M. Jeong, J. Kim, B. Kim, J. H. Kim, J. H. Kim, K. Lee and K. Char, High-k perovskite gate oxide for modulation beyond 10^{14} cm^{-2}, unpublished.

[14] P. M. Solomon and H. Morkoc, Modulation-Doped GaAs/AlGaAs heterojunction field-effect transistors (MODFET's), ultrahigh-speed device for supercomputers, IEEE Trans. Electorn Devices **31,** 1015 (1984).

[15] T. Saku, Y. Hirayama, and Y. Horikoshi, High electron mobility in AlGaAs/GaAs modulation-doped structures, Jpn. J. Appl. Phys. **30,** 902 (1991).

[16] G. Liu, J. Wu, Y. Lu, Z. Li, Y. Song, C. Li, S. Yang, X. Liu, Q. Zhu, and Z. Wang, Scattering due to spacer layer thickness fluctuation on two dimensional electron gas in AlGaAs/GaAs modulation-doped heterostructures, J. Appl. Phys. **110,** 023705 (2011).

[17] J. P. Ibbetson, P. T. Fini, K. D. Ness, S. P. DenBaars, J. S. Speck, and U. K. Mishra, Polarization effects, surface states, and the source of electrons in AlGaN/GaN heterostructure field effect transistors, Appl. Phys. Lett. **77,** 250 (2000).

[18] Y. Takei, K. Tsutsui, W. Saito, K. Kakushima, H. Wakabayashi, and H. Iwai, Jpn, dependence of ohmic contact properties on AlGaN layer thickness for AlGaN/GaN high-electron-mobility transistors, J. Appl. Phys. **55,** 040306 (2016).

[19] J. D. Ye, S. Pannirselvam, S. T. Lim, J. F. Bi, X. W. Sun, G. Q. Lo, and K. L. Teo, Two-dimensional electron gas in Zn-polar ZnMgO/ZnO heterostructure grown by metal-organic vapor phase epitaxy, Appl. Phys. Lett. **97,** 111908 (2010).

[20] A. Savoia, D. Paparo, P. Perna, Z. Ristic, M. Salluzzo, F. Miletto Granozio, U. Scotti di Uccio, C. Richter, S. Thiel, J. Mannhart, and L. Marrucci, Polar catastrophe and electronic reconstructions at the LaAlO$_3$/SrTiO$_3$ interface: Evidence from optical second harmonic generation, Phys. Rev. B **80,** 075110 (2009).

[21] W. Siemons, G. Koster, H. Yamamoto, W. A. Harrison, G. Lucovsky, T. H. Geballe, D. H. A. Blank, and M. R. Beasley, Origin of Charge Density at LaAlO$_3$ on SrTiO$_3$ Heterointerfaces: Possibility of Intrinsic Doping, Phys. Rev. Lett. **98,** 196802 (2007).

[22] H. J. Kim, U. Kim, H. M. Kim, T. H. Kim, H. S. Mun, B.-G. Jeon, K. T. Hong, W.-J. Lee, C. Ju, K. H. Kim, and K. Char, High mobility in a stable transparent perovskite oxide, Appl. Phys. Express **5,** 061102 (2012).

[23] Y. M. Kim, T. Markurt, Y. Kim, M. Zupancic, J. Shin, M. Albrecht, and K. Char, Interface polarization model for a 2-dimensional electron gas at the BaSnO$_3$/LaInO$_3$ interface, Sci. Rep. **9,** 16202 (2019).

[24] D. Jena, Ph.D. thesis, University of California, Santa Barbara, 2003.

[25] Y. M. Kim, Y. Kim, and K. Char, The role of coherent epitaxy in forming a two-dimensional electron gas at LaIn$_{1-x}$Ga$_x$O$_3$/BaSnO$_3$ interfaces, Commun. Mater. **2,** 73 (2021).

[26] E. B. Ramayya and I. Knezevic, Self-consistent Poisson-Schrödinger-Monte Carlo solver: Electron mobility in silicon nanowires, J. Comput. Electron. **9,** 206 (2010).

[27] J.-F. Mennemann, A. Jüngel, and H. Kosina, Transient Schrödinger–Poisson simulations of a high-frequency resonant tunneling diode oscillator, J. Comput. Phys. **239,** 187 (2013).

[28] M. Pourfath, H. Kosina, and S. Selberherr, A fast and stable Poisson–Schrödinger solver for the analysis of carbon nanotube transistors, J. Comput. Electron. **5,** 155 (2006).

[29] I.-H. Tan, G. L. Snider, L. D. Chang, and E. L. Hu, A self-consistent solution of Schrödinger–Poisson equations using a nonuniform mesh, J. Appl. Phys. **68,** 4071 (1990).

[30] H. Choi, M. Kim, J.-Y. Moon, J.-H. Lee, and S.-K. Son, One-dimensional Poisson calculation for electrically controlled band bending in GaAs/AlGaAs heterostructure, J. Nanosci. Nanotechnol. **20,** 4428 (2020).

[31] T. Scheinert, T. Mikolajick, and S. Schmult, Critical parameters for the presence of a 2DEG in GaN/Al$_x$Ga$_{1-x}$N heterostructures, AIP Adv. **9,** 125018 (2019).

[32] R. Singh, M. A. Khan, and S. Mukherjee, Analytical model for 2DEG density in graded MgZnO/ZnO heterostructures with Cap layer, IEEE Trans. Electron Devices **64,** 3661 (2017).

[33] I. A. Larkin and J. H. Davies, Edge of the two-dimensional electron gas in a gated heterostructure, Phys. Rev. B **52,** 5535(R) (1995).

[34] A. M. Cruz Serra and H. Abreu Santos, A one-dimensional, self-consistent numerical solution of Schrödinger and Poisson equations, J. Appl. Phys. **70,** 2734 (1991).

[35] B. Sarikavak-Lisesivdin, Numerical optimization of two-dimensional electron gas in Mg$_x$Zn$_{1-x}$O/ZnO heterostructures $(0.10 < x < 0.30)$, Philos. Mag. **93,** 1124 (2013).

[36] S. Sasa, T. Tamaki, K. Koike, M. Yano, and M. Inoue, Origin of high-density two-dimensional electron gas in ZnO/ZnMgO heterostructures, J. Phys.: Conf. Ser. **109,** 012030 (2008).

[37] A. Janotti, L. Bjaalie, L. Gordon, and C. G. Van de Walle, Controlling the density of the two-dimensional electron gas at the SrTiO$_3$/LaAlO$_3$ interface, Phys. Rev. B **86,** 241108(R) (2012).

[38] S. Su, J. H. You, and C. Lee, Electron transport at interface of $LaAlO_3$ and $SrTiO_3$ band insulators, J. Appl. Phys. **113,** 093709 (2013).

[39] K. Krishnaswamy, L. Bjaalie, B. Himmetoglu, A. Janotti, L. Gordon, and Chris G. Van de Walle, $Basno_3$ as a channel material in perovskite oxide heterostructures, Appl. Phys. Lett. **108,** 083501 (2016).

[40] J. Shin, Y. M. Kim, Y. Kim, C. Park, and K. Char, High mobility $BaSnO_3$ films and field effect transistors on non-perovskite MgO substrate, Appl. Phys. Lett. **109,** 262102 (2016).

[41] A. V. Sanchela, T. Onozato, B. Feng, Y. Ikuhara, and H. Ohta, Thermopower modulation clarification of the intrinsic effective mass in transparent oxide semiconductor $BaSnO_3$, Phys. Rev. Mater. **1,** 034603 (2017).

[42] C. Lau, Y. Kim, S. Albright, K. Char, C. H. Ahn, and F. J. Walker, Structural characterization of the $LaInO_3/BaSnO_3$ interface via synchrotron scattering, APL Mater. **7,** 031108 (2019).

[43] C. J. Roh, M.-C. Jung, J. R. Kim, K.-J. Go, J. Kim, H. J. Oh, Y.-R. Jo, Y. J. Shin, J. G. Choi, B.-J. Kim, D. Y. Noh, S.-Y. Choi, T. W. Noh, M. J. Han, and J. S. Lee, Polar metal phase induced by oxygen octahedral network relaxation in oxide thin films, Small **16,** 2003055 (2020).

[44] H. M. Park, H. J. Lee, S. H. Park, and H. I. Yoo, Lanthanum indium oxide from x-ray powder diffraction, Acta Cryst. C **59,** i131 (2003).

[45] A. Slassi, Ab initio study of a cubic perovskite: Structural, electronic, optical and electrical properties of native, lanthanum-and antimony-doped barium tin oxide, Mater. Sci. Semicond. Process **32,** 100 (2015).

[46] U. Kim, C. Park, T. Ha, R. Kim, H. S. Mun, H. M. Kim, H. J. Kim, T. H. Kim, N. Kim, J. Yu, K. H. Kim, J. H. Kim, and K. Char, Dopant-site-dependent scattering by dislocations in epitaxial films of perovskite semiconductor $BaSnO_3$, APL Mater. **2,** 056107 (2014).

[47] P. Singh, B. J. Brandenburg, C. P. Sebastian, P. Singh, S. Singh, D. Kumar, O. Parkash, and Electronic Structure, Electrical and dielectric properties of $BaSnO_3$ below 300 K, Jpn. J. Appl. Phys. **47,** 3540 (2008).

[48] H. J. Kim, U. Kim, T. H. Kim, J. Kim, H. M. Kim, B.-G. Jeon, W.-J. Lee, H. S. Mun, K. T. Hong, J. Yu, K. Char, and K. H. Kim, Physical properties of transparent perovskite oxides $(Ba,La)SnO_3$ with high electrical mobility at room temperature, Phys. Rev. B **86,** 165205 (2012).

[49] U. Kim, C. Park, T. Ha, Y. M. Kim, N. Kim, C. Ju, J. Park, J. Yu, J. H. Kim, and K. Char, All-perovskite transparent high mobility field effect using epitaxial $BaSnO_3$ and $LaInO_3$, APL Mater. **3,** 036101 (2015).

[50] K. Xiong, J. Robertson, and S. J. Clark, Defect states in the high-dielectric-constant gate oxide $LaAlO_3$, Appl. Phys. Lett. **89,** 022907 (2006).

[51] L. Yu and A. Zunger, A polarity-induced defect mechanism for conductivity and magnetism at polar–nonpolar oxide interfaces, Nat. Commun. **5,** 5118 (2014).

[52] Y. Liu, Y. Zhou, D. Jia, J. Zhao, B. Wang, Y. Cui, Q. Li, and B. Liu, Composition dependent intrinsic defect structures in $ASnO_3$ (A = Ca, Sr, Ba), J Mater. Sci. Technol. **42,** 212 (2020).

[53] Y. Kim, H. Cho, and K. Char, Fermi level pinning and band bending in δ-doped $BaSnO_3$, Appl. Phys. Lett. **118,** 052101 (2021).

[54] W. Zhong, R. D. King-Smith, and D. Vanderbilt, Giant LO-TO Splittings in Perovskite Ferroelectrics, Phys. Rev. Lett. **72,** 3618 (1994).

[55] H. E. Weaver, Dielectric properties of single crystals of $SrTiO_3$ at low temperatures, J. Phys. Chem. Solids **11,** 274 (1959).

[56] W. Nunn, A. Prakash, A. Bhowmik, R. Haislmaier, J. Yue, J. M. G. Lastra, and B. Jalan, Frequency- and temperature-dependent dielectric response in hybrid molecular beam epitaxy-grown $BaSnO_3$ films, APL Mater. **6,** 066107 (2018).

[57] D. H. Jang, W.-J. Lee, E. Sohn, H. J. Kim, D. Seo, J.-Y. Park, E. J. Choi, and K. H. Kim, Single crystal growth and optical properties of a transparent perovskite oxide $LaInO_3$, J. Appl. Phys. **121,** 125109 (2017).

[58] Rylan J. Terry, Nick Combs, Colin D. Mcmillen, Susanne Stemmer, and Joseph Kolis, Hydrothermal growth of $BaSnO_3$ single crystals for wide bandgap applications, J. Cryst. Growth **536,** 125529 (2020).

[59] C. Guguschev, D. Klimm, M. Brützam, T. M. Gesing, M. Gogolin, H. Paik, A. Dittmar, V. J. Fratello, and D. G. Schlom, Single crystal growth and characterization of Ba_2ScNbO_6 – A novel substrate for $BaSnO_3$ films, J. Cryst. Growth **528,** 125263 (2019).

[60] Z. Galazka, *et al.*, Melt growth and physical properties of bulk $LaInO_3$ single crystals, Phys. Status Solidi A **218,** 2100016 (2021).

[61] S. Adachi, GaAs, AlAs, and $Al_xGa_{1−x}$As: Material parameters for use in research and device applications, J. Appl. Phys. **58,** R1 (1985).

[62] S. M. Sze and K. K. Ng, *Physics of Semiconductor Devices* (Wiley, New York, 2006).

[63] T. Kozawa, T. Mori, T. Ohwaki, Y. Taga, and N. Sawaki, UV photoemission study of AlGaN grown by metalorganic vapor phase epitaxy, Jpn. J. Appl. Phys. **39,** 772 (2000).

[64] R. Núñez-González, A. Reyes-Serrato, A. Posada-Amarillas, and D. H. Galván, First-principles calculation of the band gap of $Al_xGa_{1−x}$N and $In_xGa_{1−x}$N, Rev. Mex. Fis. S **54,** 111 (2008).

[65] Y.-N. Xu and W. Y. Ching, Electronic, optical, and structural properties of some wurtzite crystals, Phys. Rev. B **48,** 4335 (1993).

[66] A. T. Collins, E. C. Lightowlers, and P. J. Dean, Lattice vibration spectra of aluminum nitride, Phys. Rev. **158,** 833 (1967).

[67] Z. Li, P. Wang, J. He, H. Chen, and J. Cheng, Effect of polarization on the performance of ZnO/MgZnO quantum cascade detector, Superlattices Microstruct. **111,** 852 (2017).

[68] J. G. Lu, S. Fujita, T. Kawaharamura, H. Nishinaka, Y. Kamada, and T. Ohshima, Carrier concentration induced band-gap shift in Al-doped $Zn_{1−x}Mg_x$O thin films, Appl. Phys. Lett. **89,** 262107 (2006).

[69] A. Tsukazaki, A. Ohtomo, T. Kita, Y. Ohno, H. Ohno, and M. Kawasaki, Quantum Hall effect in polar oxide heterostructures, Science **315,** 1388 (2007).

[70] H. Yin, J. Chen, Y. Wang, J. Wang, and H. Guo, Composition dependent band offsets of ZnO and its ternary alloys, Sci. Rep. **7**, 41567 (2017).

[71] H. Tampo, H. Shibata, K. Maejima, A. Yamada, K. Matsubara, P. Fons, S. Kashiwaya, S. Niki, Y. Chiba, T. Wakamatsu, and H. Kanie, Polarization-induced two-dimensional electron gases in ZnMgO/ZnO heterostructures, Appl. Phys. Lett. **93**, 202104 (2008).

[72] B. A. Lombos, Deep levels in semiconductors, Can. J. Chem. **63**, 1666 (1985).

[73] M. O. Watanabe, K. Morizuka, M. Mashita, Y. Ashizawa, and Y. Zohta, Donor levels in Si-doped AlGaAs grown by MBE, Jpn. J. Appl. Phys. **23**, L103 (1984).

[74] M. M. Sobolev, F. Y. Soldatenkov, and V. A. Kozlov, Study of deep levels in GaAs p–i–n structures, Semiconductors **50**, 924 (2016).

[75] B. Vinter, Subbands and charge control in a two-dimensional electron gas field-effect transistor, Appl. Phys. Lett. **44**, 307 (1984).

[76] M. J. Uren, K. J. Nash, R. S. Balmer, T. Martin, E. Morvan, N. Caillas, S. L. Delage, D. Ducatteau, B. Grimbert, and J. C. De Jaeger, Punch-Through in short-channel AlGaN/GaN HFETs, IEEE Trans. Electron Devices **53**, 395 (2006).

[77] T. T. Duc, G. Pozina, E. Janzén, and C. Hemmingsson, Investigation of deep levels in bulk GaN material grown by halide vapor phase epitaxy, J. Appl. Phys. **114**, 153702 (2013).

[78] Z. Xie, Y. Sui, J. Buckeridge, C. R. A. Catlow, T. W. Keal, P. Sherwood, A. Walsh, M. R. Farrow, D. O. Scanlon, S. M. Woodley, and A. A. Sokol, Donor and acceptor characteristics of native point defects in GaN, J. Phys. D: Appl. Phys. **52**, 335104 (2019).

[79] D. C. Look, Recent advances in ZnO materials and devices, Mater. Sci. Eng., B **80**, 383 (2001).

[80] H. von Wenckstern, R. Pickenhain, H. Schmidt, M. Brandt, G. Biehne, M. Lorenz, M. Grundmann, and G. Brauer, Deep acceptor states in ZnO single crystals, Appl. Phys. Lett. **89**, 092122 (2006).

[81] M. Higashiwaki, S. Chowdhury, M.-S. Miao, B. L. Swenson, C. G. Van de Walle, and U. K. Mishra, Distribution of donor states on etched surface of AlGaN/GaN heterostructures, J. Appl. Phys. **108**, 063719 (2010).

[82] J. Ghosh, in *International Conference on Electron Devices and Solid-State Circuits (EDSSC)* (2017), pp. 1–4.

[83] N. Goyal, B. Iñiguez, and T. A. Fjeldly, Analytical modeling of bare surface barrier height and charge density in AlGaN/GaN heterostructures, Appl. Phys. Lett. **101**, 103505 (2012).